

## Article

# Fluid Inclusions and Stable Isotope Geochemistry of Gold Mineralization Associated with Fine-Grained Granite: A Case Study of the Xiawolong Gold Deposit, Jiaodong Peninsula, China

Junyang Lv <sup>1,2</sup>, Zhongliang Wang <sup>3,\*</sup>, Zhengjiang Ding <sup>1,2</sup>, Rifeng Zhang <sup>3</sup>, Mingling Zhou <sup>1,2</sup>, Mingchao Wu <sup>3</sup>, Zhongyi Bao <sup>1,2</sup> and Fei Teng <sup>1</sup>

<sup>1</sup> Shandong Provincial No. 6 Exploration Institute of Geology and Mineral Resources, Weihai 264209, China; junyanglv@163.com (J.L.); ytdzhj@126.com (Z.D.); lyzhouml@126.com (M.Z.); gybzy2005@126.com (Z.B.); phoebe\_tf@163.com (F.T.)

<sup>2</sup> Shandong Provincial Engineering Laboratory of Application and Development of Big Data for Deep Gold Exploration, Weihai 264209, China

<sup>3</sup> School of Earth Sciences and Resources, China University of Geosciences, Beijing 100083, China; hovlfandsolargod@163.com (R.Z.); chunyouyuyuan@126.com (M.W.)

\* Correspondence: zhong.liangw@163.com; Tel.: +86-10-82336549; Fax: +86-10-82322175

**Abstract:** The Xiawolong gold deposit, located in the Muping–Rushan gold metallogenic belt (eastern Jiaodong Peninsula), is a newly discovered deposit that developed in the late Early Cretaceous as fine-grained granite. Gold mineralization, which mainly occurs in the middle of fresh fine-grained granite dikes, consists of stockwork-style and disseminated ores. They are characterized by middle-high-temperature mineral assemblages, such as molybdenite and magnetite, associated with gold-bearing pyrite. Four types of primary fluid inclusions, contained within the quartz grains from the gold-bearing disseminated and stockwork-style fine-grained granitic ores, were identified based on microthermometry and Raman spectroscopy. The types identified were type 1 aqueous inclusions with middle-high temperature (201 to 480 °C) and middle-low salinity of 0.18 to 17.00 wt.% NaCl equiv.; type 2 H<sub>2</sub>O–CO<sub>2</sub> inclusions, which show middle-high temperatures (218 to 385 °C), middle-low salinities (1.23 to 13.26 wt.% equiv. NaCl), and variable XCO<sub>2</sub> (0.031 to 0.044); type 3 daughter mineral-bearing inclusions with high temperature (416 to 446 °C) and relatively constant and high salinity (28.59 to 32.87 wt.% NaCl equiv.); and type 4 CO<sub>2</sub> fluid inclusions, which possess a bulk density of 0.405 to 0.758 g/cm<sup>3</sup> and a constant XCO<sub>2</sub> (0.952 to 0.990) (according to the decreasing abundance of fluid inclusions). The δ<sup>18</sup>O<sub>water</sub> range is between 3.4 and 5.9‰, and the range of the δD is from –97.1 to –77.4‰, which indicates that the ore-forming process is of a magmatic water origin. The δ<sup>34</sup>S values possess a narrow range between 4.5 and 9.3‰, indicating the source of the Mesozoic Kunyushan granitoids. The Pb isotopic compositions of pyrite show that the Mesozoic Kunyushan granitoids are the main lead source for pyrites. Types 1, 2, and 3 fluid inclusions coexist in the same view field of the quartz grain, which are suggested to occur as the result of fluid immiscibility because of the boiling of a single homogeneous NaCl–CaCl<sub>2</sub>–KCl–CO<sub>2</sub>–H<sub>2</sub>O system. The fluid immiscibility, rather the fluid mixing and wall-rock sulfidation, is the mechanism of gold precipitation in the Xiawolong deposit. Compared with both the “Linglong-type” and “Jiaojia-type” gold deposits in the Jiaodong Peninsula in terms of geological–petrographic evidence and all of the available geochemical data, it can be concluded the Xiawolong gold deposit is of magmatic hydrothermal origin, having a genetic relation to the fine-grained granite.

**Keywords:** Xiawolong gold deposit; Jiaodong Peninsula; fine-grained granite; fluid inclusions



**Citation:** Lv, J.; Wang, Z.; Ding, Z.; Zhang, R.; Zhou, M.; Wu, M.; Bao, Z.; Teng, F. Fluid Inclusions and Stable Isotope Geochemistry of Gold Mineralization Associated with Fine-Grained Granite: A Case Study of the Xiawolong Gold Deposit, Jiaodong Peninsula, China. *Appl. Sci.* **2022**, *12*, 7147. <https://doi.org/10.3390/app12147147>

Academic Editor: Dibyendu Sarkar

Received: 18 June 2022

Accepted: 13 July 2022

Published: 15 July 2022

**Publisher's Note:** MDPI stays neutral with regard to jurisdictional claims in published maps and institutional affiliations.



**Copyright:** © 2022 by the authors. Licensee MDPI, Basel, Switzerland. This article is an open access article distributed under the terms and conditions of the Creative Commons Attribution (CC BY) license (<https://creativecommons.org/licenses/by/4.0/>).

## 1. Introduction

The Jiaodong Peninsula, situated at the southeastern edge of the North China Craton (NCC) (Figure 1) [1], is endowed with a total proved reserve of over 5000 t Au [2], which makes it one of the most important gold provinces worldwide, and the number one gold producer in China (Figure 1) [3,4]. The giant Jiaodong gold province is composed of the Zhaoyuan–Laizhou, Penglai–Qixia, and Muping–Rushan gold metallogenic belts situated in the western, central, and eastern Jiaodong Peninsula, respectively (Figure 1) [5].

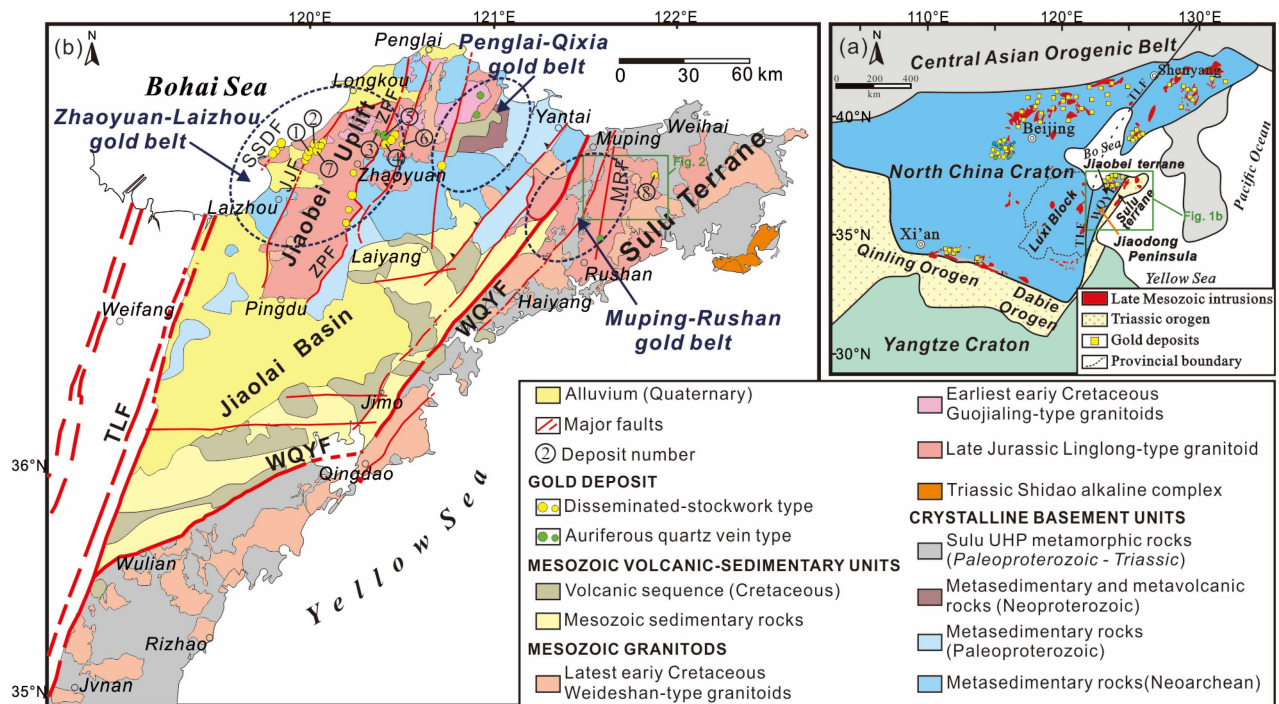


**Figure 1.** (a) A simplified tectonic map of the North China craton showing the location of the Jiaodong Peninsula. Adapted with permission from Ref. [6]. 2012, Elsevier. (b) A simplified geological map of the Jiaodong Peninsula showing the distribution of crystalline basement, Mesozoic volcanic-sedimentary sequence and granitoids, major structures, and typical gold deposits. Adapted with permission from Ref. [1]. 2015, Elsevier. Main faults: WQYF, Wulian–Qingdao–Yantai Fault; TLF, Tan–Lu Fault; ZPF, Zhaoping Fault; SSDF, Sanshandao Fault; JJF, Jiaojia Fault; MRF, Muping–Rushan Fault. Typical gold deposits: ① Jiaojia; ② Xincheng; ③ Linglong; ④ Taishang; ⑤ Fushan; ⑥ Luoshan; ⑦ Wang’ershan; ⑧ Xiawolong.

Since the 1980s, a large number of studies have been performed on the Jiaodong gold deposits in terms of the source of ore-forming fluids [7,8], the timing of gold deposition [9–11], the structural environment controlling the auriferous fluid migration [12,13], the hydrothermal alteration [14,15], and the metallogenic geodynamic setting [16–18]. The gold deposits, with the Precambrian high-grade metamorphic rocks of the NCC, the late Jurassic Linglong-type granitoids, and the middle Early Cretaceous Guojialing-type granitoids being the gold-hosting rocks, are considered to occur as two types of mineralization, i.e., the “Jiaojia-type” and the “Linglong-type” [1]. The former is represented by the gold-bearing quartz veins, and the latter is represented by stockwork and disseminated pyrite-sericite–quartz altered ores [19,20]. The “Jiaojia-type” gold deposit is generally hosted in the regional NNE- to NE-trending faults along the lithologic contacts between Linglong granite and Precambrian metamorphic rock or between Linglong granite and Guojialing-type granitoid, such as the Sanshandao, Jiaojia, and Zhaoping faults (Figure 1b) [21], and “Linglong-type” deposit is usually hosted in the lower-order NNE- to NE-trending faults that cut the Mesozoic granitoids or the Precambrian metamorphic rocks (Figure 1b) [22]. Both of the two types of orebodies are surrounded by the zoned hydrothermal alteration

characterized by strong sericitization in the inner domain and silicification in the outer. The thickness of the alteration envelope is usually between 10 and several hundred meters for the “Jiaojia-type” gold deposit, and less than 2 m for the “Linglong-type” deposit [23].

However, a special case is the Xiawolong gold deposit, situated at the Muping–Rushan gold metallogenic belt (Figure 1). It was newly discovered by the Shandong Provincial No.6 Exploration Institute of Geology and Mineral Resources, China during 2012–2017 [24]. Based on the primary geological survey work, the deposit is different from both the “Linglong-type” and “Jiaojia-type” gold deposits in terms of host rock, gold mineralization style, structural controls, and hydrothermal alteration [24]. Furthermore, so far, no more information has been published on this deposit.

More interestingly, it is noted that the deposit developed in the late Early Cretaceous as fine-grained granite. Fine-grained granite is considered to be the late-stage product of granitic magmatic crystallization and is usually rich in Be–Li–Nb–Ta–Sn–Bi–W–Mo–Cu–Zn–U elements [25–28], which has resulted in the close spatial and temporal relationship between fine-grained granites and orebodies in many deposits [29], such as the W–Mo deposit [28,30,31], copper deposit [32], uranium deposit [25,33,34], and Pb–Zn deposit [35]. However, little information on the gold mineralization associated with fine-grained granite has been reported to date.

This paper reports the fluid inclusions and stable isotope geochemistry of Xiawolong gold deposit and draws comparisons with the ore-forming fluid geochemistry of the “Linglong-type” and “Jiaojia-type” gold deposits in the Jiaodong Peninsula, in order to reveal the ore-forming characteristics of gold mineralization associated with the fine-grained granite, and discuss whether the distinct mineralization styles were formed under the different or similar ore-forming processes. The present work sheds new light on the genesis of gold in the Jiaodong gold deposits.

## 2. Geological Setting and Ore Deposit Geology

### 2.1. Geological Setting

The Jiaodong Peninsula, to the west separated from the Luxi Block of the NCC by the 2400 km long NNE–SSW (010° and 025°) trending and steeply dipping Tan–Lu Fault (TLF), and to the east bounded by the Pacific Plate [36], consists of the Sulu terrane in the southeast and the Jiaobei terrane in the northwest (Figure 1a). The Jiaobei and Sulu terranes are separated by the lithospheric-scale NNE–SSW- to NE–SW-trending Wulian–Qingdao–Yantai Fault (WQYF) (Figure 1a,b). The former includes the Jiaolai Basin in the southeast and the Jiaobei Uplift in the northwest (Figure 1b) [37], where all the gold deposits are hosted by the Jiaobei Uplift. More precisely, the Zhaoyuan–Laizhou and Penglai–Qixia gold metallogenic belts are located in the western and central Jiaodong Peninsula, respectively (Figure 1) [5], whereas in the Sulu Terrane, namely the eastern Jiaodong Peninsula, gold is concentrated in the Muping–Rushan gold metallogenic belt (Figure 1) [5].

The Muping–Rushan gold metallogenic belt is dominated by Paleoproterozoic and Neoproterozoic basement rocks of the Yangtze Craton (YC) [38], which were subjected to an ultrahigh-pressure (UHP) metamorphic event resulting from the mid-Late Triassic collision ca. 244 to 220 Ma between the YC and NCC along the WQYF [39], as well as the Mesozoic intrusions (Figures 2 and 3) [37]. The UHP metamorphic rocks comprise quartzite, coesite-bearing eclogite, granitic gneiss, and marble [40], with the granulite to amphibolite-facies metamorphism (220 to 205 Ma) overprinting in local outcrops [41]. The Late Jurassic–Early Cretaceous magmatism was widely developed (Figure 2) [42], of which the Late Jurassic crustally derived Kunyushan granitoid, with emplacement ages ranging between 161 and 141 Ma [43,44], is a batholith consisting of granodiorite, monzogranite, and garnet-bearing leucogranite [45], whereas the late Early Cretaceous Sanfoshan monzonite resulting from crust–mantle interaction, with zircon U–Pb ages varying from 121 to 110 Ma [45], which intrudes into the Kunyushan granitoid in the southeast part (Figure 2). The former is undeformed and hosts no gold deposits, whereas the latter exhibits an NNE–SSW-trending

mylonitic foliation associated with WNW–ESE-trending stretching lineations [42] and hosts almost all the gold deposits in the Muping–Rushan gold metallogenic belt (Figure 2).

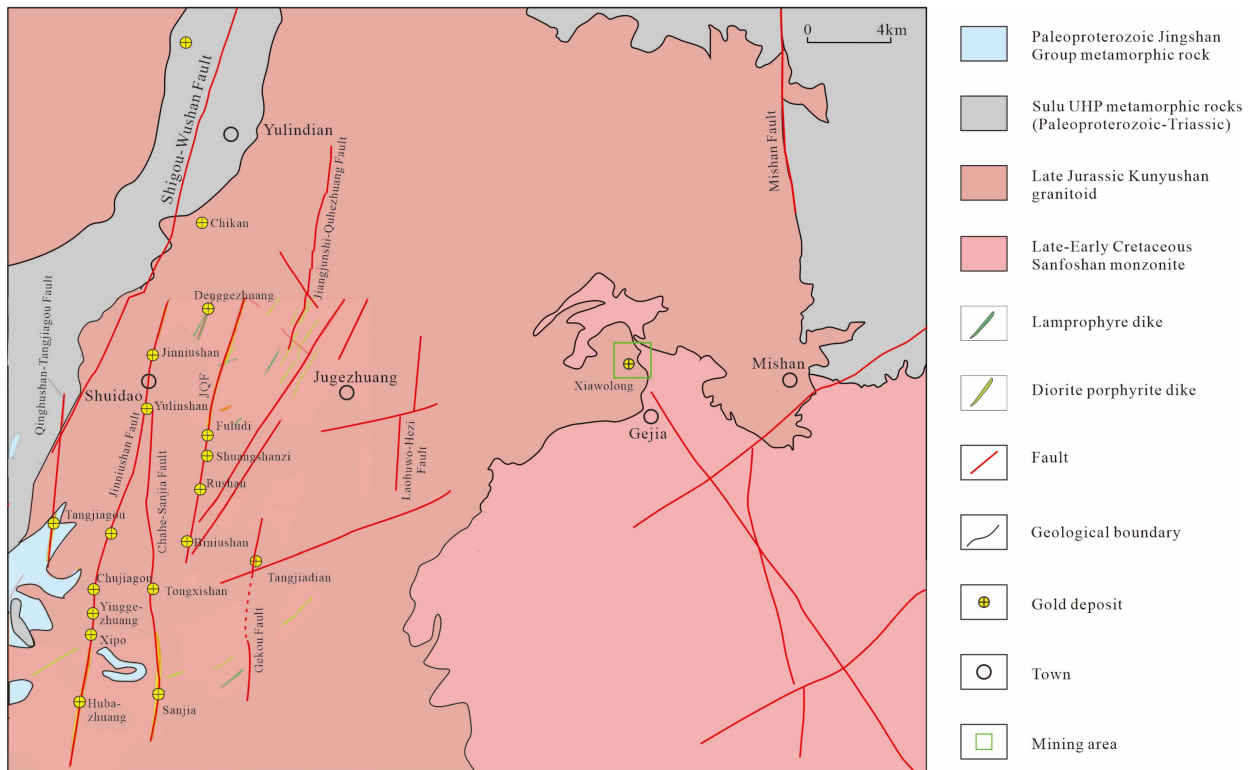


**Figure 2.** Geological map of the Muping–Rushan gold belt. Adapted with permission from Ref. [46]. 2007, Elsevier.

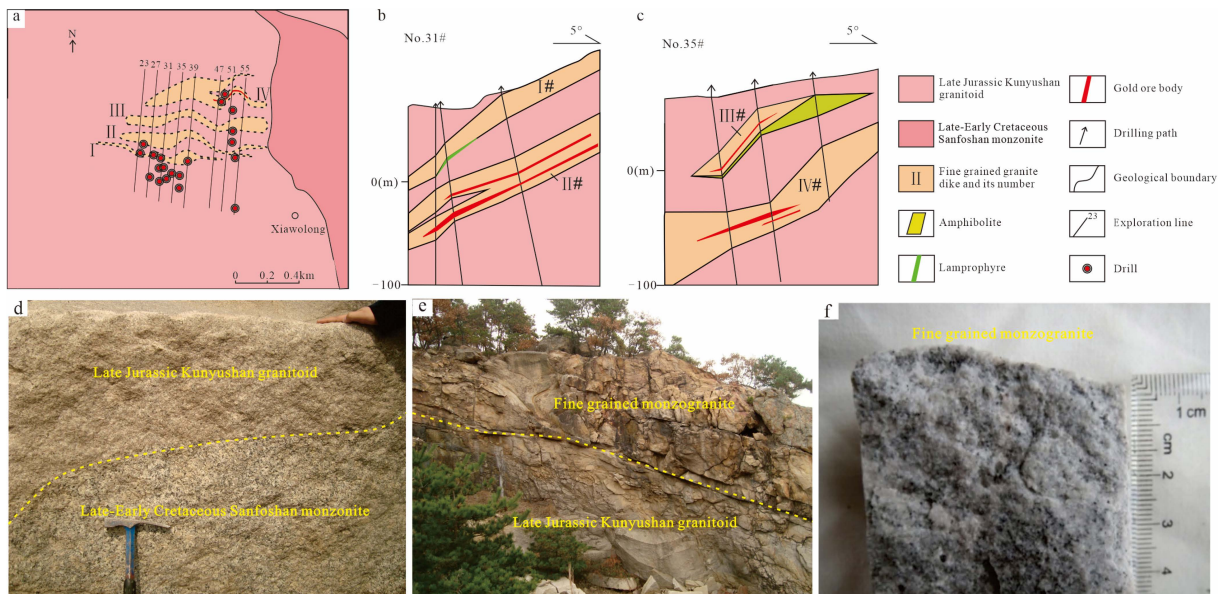


**Figure 3.** (a) Geological map of the Xiawolong gold deposit. (b) No. 31# and (c) No. 35# prospecting line profile of the Xiawolong gold deposit. (d) The abrupt contact between the medium- to coarse-grained monzogranite and medium- to fine-grained monzonite. (e) The abrupt contact between the medium- to coarse-grained monzogranite and the fine-grained granite dike. (f) Unaltered fine-grained granite.

Structurally, the Muping–Rushan gold metallogenic belt is dominated by the NNE–NE-trending Muping–Rushan Fault Zone, as well as the SN-trending Mishan Fault, considered to be subsidiary to the WQYF [47] (Figures 1 and 2). The Muping–Rushan Fault Zone comprises a series of sub-parallel NNE–NE-striking faults steeply dipping towards the SE (Figure 2), which are evenly distributed with an interval of ca. 2–3 km in the middle to central part of the Kunyushan granitoid, from west to east, named the Qinghushan–Tangjiagou, Jinniushan, Chahe–Sanjia, Jiangjunshi–Quhezhuang, Gekou, and Laohuwo–Hezi Faults. These faults, usually ca. 5 to 15 km long, cut the Late Jurassic Kunyushan granitoids at the footwall of the WQYF and control the “Linglong-type” deposits, represented by the Jinqingding, Denggezhuang, and Yinggezhuang gold deposits, whereas the Mishan Fault, striking N5° and dipping E 40 to 65°, mostly follows the contact between the east edge of the Kunyushan granitoid in the footwall and the UHP metamorphic rocks in the hanging wall (Figure 2). This area underwent multiple tectonic movements, with mylonites, cataclastic, fault gouge, and weak hydrothermal alteration occurring along the fault; however, no gold deposits have yet been discovered within it [24].

## 2.2. Ore Deposit Geology

The Xiawolong gold deposit, 20 km or so northeast of the Jinqingding gold deposit, is situated along the contact between the Sanfoshan granitic pluton and the Kunyushan granitoid in the southeast part of the Muping–Rushan gold metallogenic belt (Figure 2). It is dominated by Kunyushan monzogranite, where both the UHP metamorphic rocks and Paleoproterozoic Jingshan Group metamorphic rocks occur as discrete ellipsoidal xenoliths, as well as the Sanfoshan granitic pluton (Figure 3a–c). The Sanfoshan granitic pluton, a sheet-like NNW-trending intrusive body of medium- to fine-grained monzonite, intrudes the medium- to coarse-grained Kunyushan monzogranite (Figures 2 and 3a) and shows abrupt contact with the host rock (Figure 3d).

The gold orebodies are hosted in the fine-grained granite, which mainly occurs as concealed dikes (Figure 3a–c). However, a few outcrops, showing abrupt contact with the medium- to coarse-grained Kunyushan monzogranite (Figure 3e), can be observed locally. Four fine-grained granite dikes, named I#, II#, III#, and IV#, are recognized based on a systematic drill hole in the Xiawolong gold mine (Figure 3a–c). They strike E–W, dip 20 to 50° to the S, and show varied thicknesses between 10 and 80 m (Figure 3a–c). No baked margins are observed at the contact between the Kunyushan monzogranite and fine-grained granite dike. The latter is generally fresh and non-deformed, where almost no alterations, faults, or fractures develop (Figure 3f).

A total of 19 gold orebodies have been discovered in the Xiawolong gold mine to date. All of them are concealed with a lens shape, and most are located in the middle of the fine-grained granite dikes, with only a few in the lower or upper margins (Figure 3b,c). Lode II-1#, hosted in the II# fine-grained granite dike, is the main orebody and is approximately 366 m long, which accounts for 67% of the proven resource. It usually strikes 270 to 285° and dips 20 to 28° (average 25°) SW, showing the roughly S-shaped, vein-like lenses (Figure 3b,c). It has variable thickness ranging from 0.91 to 2.85 m (average 1.17 m), extending from the +44 m level down to below the –70 m level. The gold grade ranges between 1.5 and 52.6 g/t with an average of 11.47 g/t gold.

All the gold orebodies in the Xiawolong gold mine are characterized by the disseminated and stockwork-style ores developed in the fresh fine-grained granite dikes (Figure 4a–c). The gangue minerals comprise K-feldspar, calcite, quartz, biotite, and plagioclase (Figure 4d–f), and the ore minerals mainly consist of include pyrite, magnetite, pyrrhotite, molybdenite, and chalcopyrite, with minor quantities native gold and electrum (Figure 4g–l). Calcites mostly occur as subhedral fine-grained grains intergrown with quartz, K-feldspar, and plagioclase (Figure 4d). In general, the euhedral fine-grained pyrite is associated with the subhedral and anhedral quartz, biotite, and K-feldspar (Figure 4e–g), with the K-feldspar grain hosted in pyrite (Figure 4f). It is also common that the anhedral pyrite is intergrown with quartz (Figure 4h), which is associated with anhedral magnetite,

pyrrhotine, chalcopyrite, and molybdenite (Figure 4i–k). Gold is the only economically viable element, and other elements such as S, Cu, and Mo are all sub-economic. The most important gold-bearing mineral is pyrite, followed by magnetite, pyrrhotite, chalcopyrite, and molybdenite. The gold is fine-grained (56%) and medium-grained (44%) gold, and mainly occurs on the margins of the individual grains (60%) (Figure 4l) or as inclusions in pyrite and other sulfides (35%), with only a few as filling microfractures in pyrite (5%).

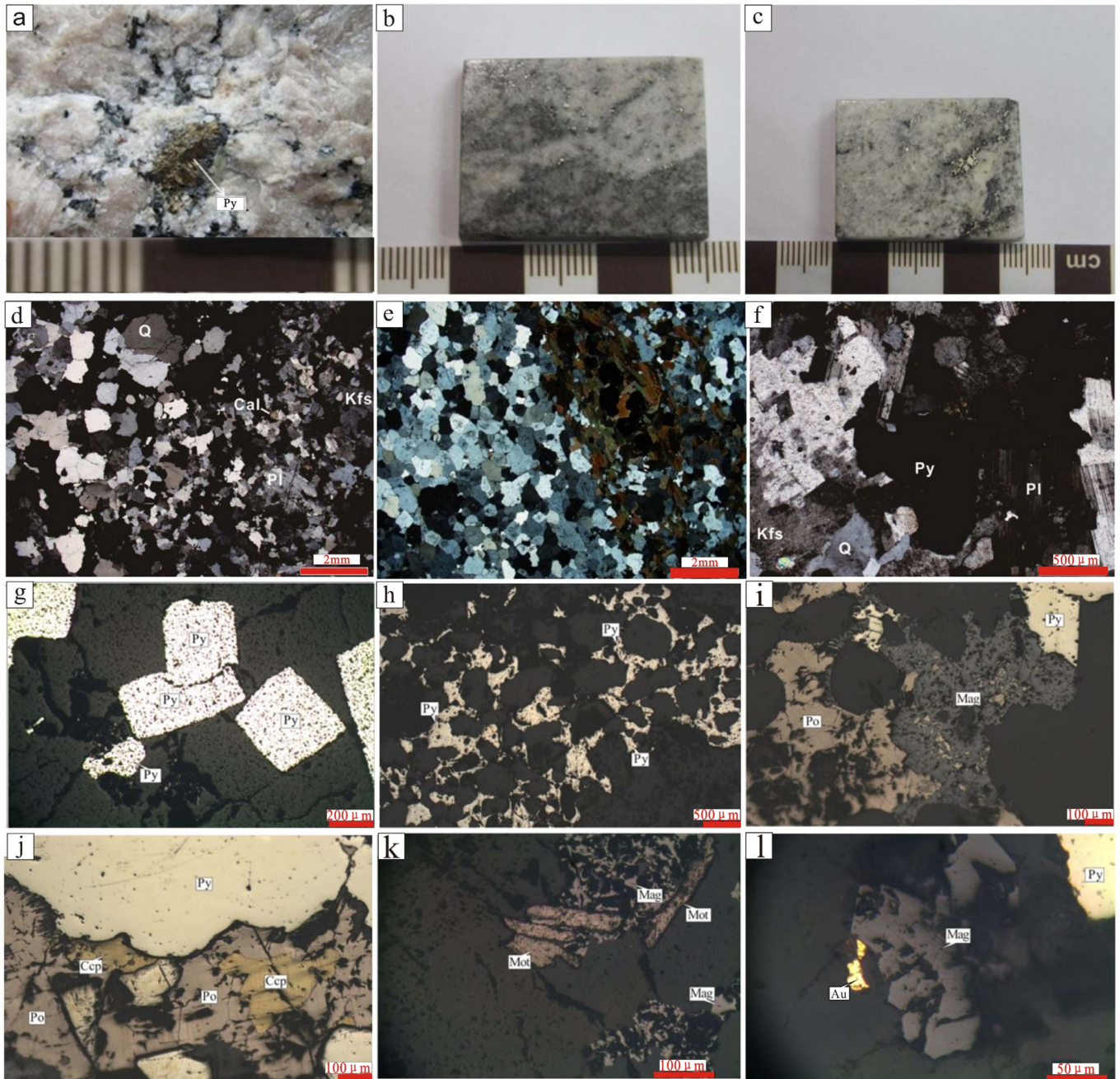


**Figure 4.** Photographs of (a,b) disseminated and (c) fine-grained granite dikes. Photomicrographs under transmitted light (d–f) and reflected light (g–l), showing the important minerals, textures, and occurrences of gold at Xiawolong deposit; (d) Subhedral) stockwork-style ores developed in the fresh

and anhedral quartz, calcite, K-feldspar, and plagioclase; (e) Subhedral and anhedral quartz and biotite intergrown with pyrite; (f) subhedral and anhedral quartz, K-feldspar, and plagioclase intergrown with pyrite; (g) euhedral pyrite intergrown with quartz; (h) anhedral pyrite intergrown with quartz; (i) pyrite intergrown with magnetite and pyrrhotine; (j) pyrite intergrown with chalcopyrite and pyrrhotine; (k) anhedral molybdenite associated with magnetite; (l) gold on the margin of magnetite. Abbreviations: Qz, quartz; Bt, biotite; Cal, calcite; Kfs, K-feldspar; Pl, plagioclase; Au, gold; Py, pyrite; Mot, molybdenite; Mag, magnetite; Po, pyrrhotine; Ccp, chalcopyrite.

### 3. Sampling and Analytical Methods

#### 3.1. Fluid Inclusion Analyses

Samples were taken from the gold-bearing disseminated and stockwork-style fine-grained granitic ores for fluid inclusion analyses. Twenty-seven doubly polished sections were examined petrographically, of which twelve samples were picked for microthermometric and laser Raman spectroscopic measurement on quartzes. In disseminated fine-grained granitic ores, quartz grains occur as fine-grained (0.1 to 0.5 mm), anhedral to subhedral, and smoky gray aggregates intergrown with disseminated euhedral pyrite, magnetite, pyrrhotite, chalcopyrite, and molybdenite (Figure 5a), whereas in stockwork-style fine-grained granitic ores, they occur as euhedral fine-grained (0.2 to 0.7 mm) and dark gray veins intergrown with sulfide veins, which mainly consists of pyrite, magnetite, pyrrhotite, chalcopyrite, and molybdenite (Figure 5b). All of the samples had no deformation Figure 5a–c). The fluid inclusions trapped in the quartzes are generally minute (3 to 15  $\mu\text{m}$ ), with many of occurring as clusters, whereas a few occur in isolation (Figure 5c).

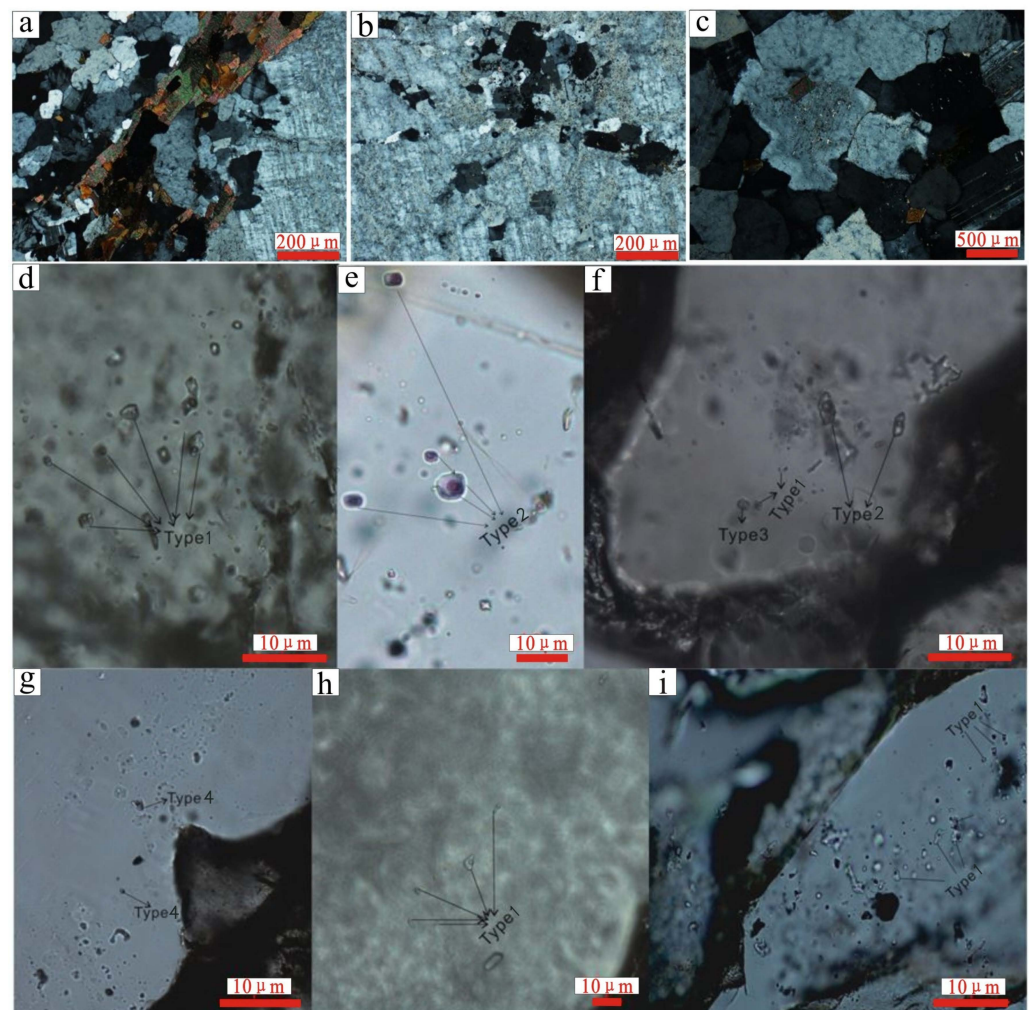


**Figure 5.** (a–c) Photomicrographs under cross-polarized light showing the micro-texture characteristics

of quartz grains for fluid inclusion studies: (a) fine-grained subhedral quartz grains intergrown with disseminated euhedral pyrite; (b) fine-grained subhedral quartz grains intergrown with sulfide vein; (c) fluid inclusions occurring as irregular, three dimensional clusters or in isolation. (d–i) Photomicrographs under plane-polarized light showing the characteristics of fluid inclusions from Xiawolong gold deposit: (d) type 1 inclusions (liquid H<sub>2</sub>O + vapor H<sub>2</sub>O) occurring as irregular, three-dimensional clusters; (e) type 2 H<sub>2</sub>O–CO<sub>2</sub> inclusions containing three phases (liquid H<sub>2</sub>O + liquid CO<sub>2</sub> + CO<sub>2</sub>-rich vapor); (f) type 3 daughter mineral-bearing inclusions coexisting with types 1 and 2 within the same field of view; (g) type 4 CO<sub>2</sub> inclusions consisting of liquid CO<sub>2</sub> and vapor CO<sub>2</sub>; (h) type 1 inclusions with elongated and irregular shapes; (i) type 1 inclusions occurring along pseudo-secondary trails. Abbreviations: Qtz, quartz; Py, pyrite.

Fluid inclusion microthermometry was performed on the Linkam THMSG 600 heating–cooling stage equipped with a Leitz microscope, the measured temperature range of which is from –198 °C to 600 °C, at the Fluid Inclusion Laboratories of China University of Geosciences, Beijing. For ensuring the accuracy of measurements, the synthetic fluid inclusions were selected to calibrate the stage. Firstly, the freezing experiments were performed so as to avoid experimentally induced stretching. Then, during the heating process, when near the clathrate-melting temperatures ( $T_{m(\text{clath})}$ ) and the melting temperatures of the carbonic phase ( $T_{m(\text{CO}_2)}$ ), the heating rate was 0.1–0.2 °C/min, and for the other measurements, it was 0.2–0.4 °C/min. Uncertainties were  $\pm 0.1$  °C and  $\pm 1$  °C for temperatures < 30 °C and >30 °C, respectively.

After the microthermometry, Laser Raman (LRM) analysis was performed at the Fluid Inclusion Laboratories of China University of Geosciences, Beijing. The LRM analysis instrument, used to collect Raman spectra of the fluid inclusion trapped in the quartz grains, was a British Renishaw inVia Raman spectrometer. The light source used was an argon ion laser, with a wavelength of 514.5 nm, a laser power of 20 mW, and a laser beam spot size of approximately 1  $\mu\text{m}$ . During the analysis, the counting time was 10 to 30 s, and the peaks were taken for one time point in the whole waveband of 100 to 4000  $\text{cm}^{-1}$ , with the spectral resolution being 1 to 2  $\text{cm}^{-1}$ . According to the measured Raman spectrum peak area and relative Raman cross-section values given by [48], i.e., 2.5 for CO<sub>2</sub> and 7.5 for CH<sub>4</sub>, the molar compositions of the fluid inclusions were obtained.

### 3.2. D-O and S-Pb Isotopic Analyses

Thirteen typical samples, from the gold-bearing disseminated and stockwork-style fine-grained granitic ores, were crushed to 40–60 mesh in order to separate the pyrite and quartz. For the quartz and pyrite, >99% purity was obtained by handpicking under a binocular microscope, and they were then used for D-O and S-Pb isotopic studies, respectively, at the Analytical Laboratory of the Beijing Research Institute of Uranium Geology.

For D isotopic analysis, quartz grains were heated to over 600 °C in an induction furnace to release the water from fluid inclusions inside the quartzes, which was then converted to H<sub>2</sub> by reacting with zinc powder at ca. 400 °C. Regarding the O isotopic analysis, the quartz grains were first reacted with BrF<sub>5</sub> at 500–600 °C for ca. 14 h to generate O<sub>2</sub>, and then reacted with graphite to generate CO<sub>2</sub> at ca. 700 °C. The resultant H<sub>2</sub> and CO<sub>2</sub> were measured by the Finnigan MAT-253 mass spectrometer to determine the D-O isotopic composition, which was recorded relative to the Standard Mean Ocean Water (SMOW) with a precision of  $\pm 1\%$  [49].

For S isotopic analysis, under a vacuum pressure of  $2 \times 10^{-2}$  Pa at ca. 980 °C, the pyrite grains were reacted with cuprous oxide to generate SO<sub>2</sub>, which was then measured using a Delta V Plus mass spectrometer. The S isotope composition adopted the Canyon Diablo Troilite (CDT) standards with a precision of  $\pm 0.2\%$  [49]. For Pb isotopic analysis, pyrite grains were first dissolved by HNO<sub>3</sub> and HCl, then passed through an anion exchange resin to extract the Pb, which, after drying, was diluted by 1% HNO<sub>3</sub> for testing by the ISOPROBE-T Thermal Ionization Mass Spectrometer. Pb isotope results are reported in

terms of normalization to the accepted ratio for NBS-981:  $^{208}\text{Pb}/^{204}\text{Pb} = 36.7119 \pm 0.0331$ , and  $^{207}\text{Pb}/^{204}\text{Pb} = 15.4968 \pm 0.0107$ ,  $^{206}\text{Pb}/^{204}\text{Pb} = 16.9386 \pm 0.0131$  ( $\pm 2\sigma$ ).

## 4. Fluid Inclusion Study

### 4.1. Fluid Inclusion Petrography

Based on careful petrographical observation, microthermometry at room temperature and Raman spectroscopy, four types of fluid inclusions trapped in the quartz grains related to the ore-forming event were identified, according to their phases. These types of fluid inclusions were type 1 aqueous, type 2  $\text{H}_2\text{O}-\text{CO}_2$ , type 3 daughter mineral-bearing, and type 4  $\text{CO}_2$  fluid inclusions, according to their abundance from high to low, respectively. Type 1 aqueous inclusions, generally 2–15  $\mu\text{m}$  in diameter, consist of two phases (liquid  $\text{H}_2\text{O}$  + vapor  $\text{H}_2\text{O}$ ), having a variable degree of fill (10–60 vol.% gas) (Figure 5d). They normally develop as clusters or along pseudo-secondary trails, possessing negative crystal, ellipsoid, irregular, or elongated shapes (Figure 5d,h,i). Type 2  $\text{H}_2\text{O}-\text{CO}_2$  inclusions contain three phases of liquid  $\text{H}_2\text{O}$  + liquid  $\text{CO}_2$  +  $\text{CO}_2$ -rich vapor (Figure 5e), with a  $\text{CO}_2$  volumetric proportion of 20–60% (Figure 5e). They are usually 3–15  $\mu\text{m}$  in diameter, and occur in isolation, with ellipsoid, elongated, or irregular shapes (Figure 5e). Type 3 daughter mineral-bearing inclusions are composed of one salt daughter mineral, which has a variable volume ratio of 20–60%, aqueous solution, and a vapor bubble (Figure 5f). They are generally isolated and have ellipsoid shapes, ranging from 9 to 15  $\mu\text{m}$  in diameter (Figure 5f). Type 4  $\text{CO}_2$  inclusions comprise liquid  $\text{CO}_2$  and vapor  $\text{CO}_2$ , usually showing a constant degree of fill (30–50 vol.% gas) (Figure 5g) and are typically 2 to 15  $\mu\text{m}$  in diameter (Figure 5g). They occur in isolation, with round, ellipsoid, elongated, or irregular shapes (Figure 5g).

### 4.2. Results of Microthermometry

#### 4.2.1. Type 1 Aqueous Inclusions

Although it is difficult to obtain and replicate the eutectic temperatures, i.e., the first ice melting temperatures ( $T_{\text{me}}$ ), because of the small diameter of the type 1 aqueous inclusions, some observations of  $-58.4$  to  $-51.2$   $^\circ\text{C}$  (mean  $-55 \pm 2.3$   $^\circ\text{C}$ ;  $1\sigma$ ;  $n = 9$ ) could be obtained (Table 1). Final ice melting temperatures ( $T_{\text{m(ice)}}$ ) were  $-13.0$  to  $-0.1$   $^\circ\text{C}$  (mean  $-6.3 \pm 3.4$   $^\circ\text{C}$ ;  $1\sigma$ ;  $n = 76$ ), whereas they usually range from  $-13.0$  to  $-2.0$   $^\circ\text{C}$  (mean  $-7.0 \pm 3.0$   $^\circ\text{C}$ ;  $1\sigma$ ;  $n = 67$ ). Total homogenization ( $T_{\text{h(tot)}}$ ) to liquid takes place in a wide range of temperatures, from 201 to 480  $^\circ\text{C}$  (mean  $289 \pm 71$   $^\circ\text{C}$ ;  $1\sigma$ ;  $n = 76$ ) (Table 1; Figure 6).

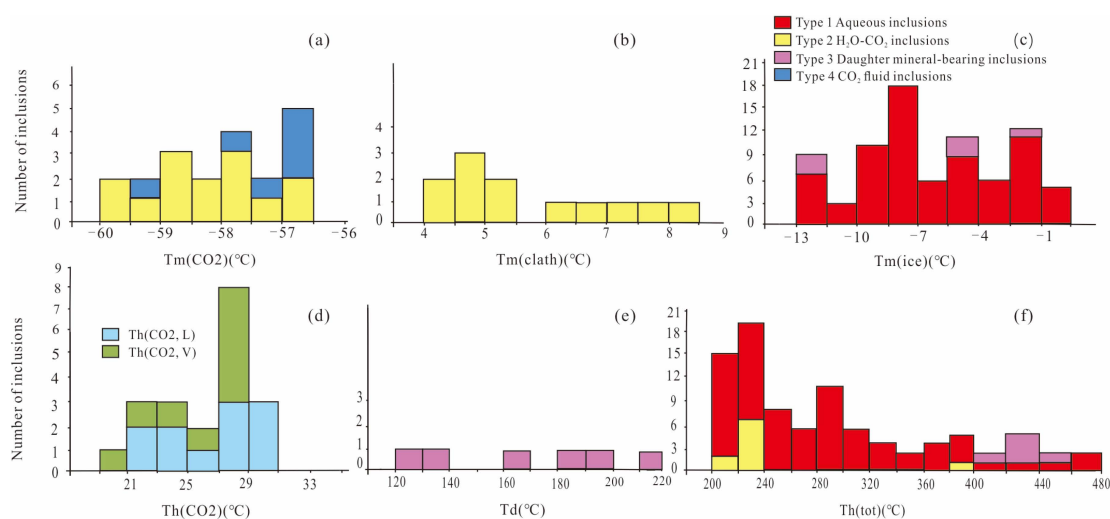


**Figure 6.** Histograms of microthermometric data including: (a) melting temperatures of  $\text{CO}_2$  ( $T_{\text{m}(\text{CO}_2)}$ ), (b) clathrate-melting temperatures ( $T_{\text{m}(\text{clath})}$ ), (c) final ice melting temperatures ( $T_{\text{m}(\text{ice})}$ ), (d) homogenization temperatures of  $\text{CO}_2$  ( $T_{\text{h}(\text{CO}_2)}$ ), (e) dissolution temperatures of halite/sylvite ( $T_{\text{d}}$ ), and (f) temperatures of total homogenization ( $T_{\text{h}(\text{tot})}$ ).

**Table 1.** Summary of the microthermometric data for fluid inclusions trapped in quartz at the Xiawolong gold deposit. Note: data are given as mean, 1 $\sigma$  standard deviation, range, and number of measurements.

Ore Style	Fluid Inclusion Type	T <sub>m</sub> CO <sub>2</sub> (°C)	T <sub>m</sub> e (°C)	T <sub>m</sub> ice (°C)	T <sub>m</sub> Clath (°C)	T <sub>h</sub> CO <sub>2</sub> (l, °C)	T <sub>h</sub> CO <sub>2</sub> (v, °C)	T <sub>d</sub> (°C)	T <sub>h</sub> TOT (°C)
disseminated	Type 1 aqueous	/	−58.4 to −51.2 (−55 ± 2.3, n = 9)	−13 to −0.3 (−6.9 ± 3.2, n = 43)	/	/	/	/	201 to 480 (283.8 ± 80.1, n = 43)
	Type 2 H <sub>2</sub> O-CO <sub>2</sub>	−56.6 to −59.1 (−58.2 ± 0.8, n = 7)	/	/	4.3 to 9.4 (6.5 ± 1.8, n = 7)	22.3 to 27.3 (24.3 ± 2.2, n = 4)	21.3 to 26.1 (23.7 ± 2, n = 3)	/	220 to 385 (257.6 ± 56.5, n = 7)
	Type 3 daughter mineral-bearing	/	/	−17.1 to −1.5 (−8.1 ± 6.6, n = 3)	/	/	/	120 to 219 (175.3 ± 41.2, n = 3)	416 to 446 (432.7 ± 12.5, n = 3)
	Type 4 CO <sub>2</sub>	−56.6 (n = 1)	/	/	/	/	20.3 (n = 1)	/	/
stockwork	Type 1 aqueous	/	/	−12.5 to −0.1 (−5.5 ± 3.7, n = 33)	/	/	/	/	202 to 390 (296.5 ± 56.7, n = 33)
	Type 2 H <sub>2</sub> O-CO <sub>2</sub>	−59.6 to −56.6 (−57.9 ± 1, n = 7)	/	/	2 to 7 (4.9 ± 1.5, n = 7)	30.2 to 30.4 (30.3 ± 0.1, n = 2)	30.1 to 30.6 (30.3 ± 0.2, n = 5)	/	218 to 289 (242 ± 22.9, n = 7)
	Type 3 daughter mineral-bearing	/	/	−11.8 to −5.1 (−7.4 ± 3.1, n = 3)	/	/	/	139 to 192 (165.3 ± 21.6, n = 3)	421 to 439 (429 ± 7.5, n = 3)
	Type 4 CO <sub>2</sub>	−59.1 to −56.6 (−56.8 ± 0.3, n = 3)	/	/	/	21.2 to 29.3 (24.6 ± 34, n = 3)	/	/	/

#### 4.2.2. Type 2 H<sub>2</sub>O–CO<sub>2</sub> Inclusions

The first melting temperatures for the type 2 H<sub>2</sub>O–CO<sub>2</sub> inclusions, i.e., carbonic phase melting temperatures ( $T_{m(\text{CO}_2)}$ ), range from  $-59.6$  to  $-56.6$  °C (mean  $-58.2 \pm 1$  °C;  $1\sigma$ ;  $n = 14$ ) (Table 1; Figure 6). Most of them are just below the pure CO<sub>2</sub> triple-point ( $-56.6$  °C), indicating that other minor quantities of gas species likely exist in the carbonic phase, such as CH<sub>4</sub> (Burruss, 1981). Clathrate-melting temperatures ( $T_{m(\text{clath})}$ ) range from  $2.0$  to  $9.4$  °C (mean  $5.7 \pm 1.8$  °C;  $1\sigma$ ;  $n = 14$ ). The partial homogenization of CO<sub>2</sub> ( $T_{h(\text{CO}_2)}$ ) into liquid takes place from  $22.3$  to  $30.4$  °C (mean  $26.8 \pm 3.1$  °C;  $1\sigma$ ;  $n = 6$ ), whereas the homogenization of inclusions into vapor occurs from  $21.3$  to  $30.6$  °C (mean  $27.8 \pm 3.4$  °C;  $1\sigma$ ;  $n = 8$ ) (Table 1; Figure 6). Total homogenization ( $T_{h(\text{tot})}$ ) to liquid for all of the H<sub>2</sub>O–CO<sub>2</sub> inclusions takes place from  $218$  to  $385$  °C (mean  $249.8 \pm 43.8$  °C;  $1\sigma$ ;  $n = 14$ ) (Table 1; Figure 6).

#### 4.2.3. Type 3 Daughter Mineral-Bearing Inclusions

For the type 3 daughter mineral-bearing inclusions, the final ice melting temperatures ( $T_{m(\text{ice})}$ ) displayed a large range from  $-17.1$  to  $-1.5$  °C (mean  $-7.7 \pm 5.2$  °C;  $1\sigma$ ;  $n = 6$ ), similar to the temperatures for the type 1 aqueous inclusions. The halite (sylvite) fully dissolved at  $120$  to  $219$  °C, with a mean value of  $170 \pm 33$  °C ( $1\sigma$ ;  $n = 6$ ) (Table 1; Figure 6), before the total homogenization ( $T_{h(\text{tot})}$ ) of these inclusions to liquid occurred at  $416$  to  $439$  °C (mean  $431 \pm 10$  °C;  $1\sigma$ ;  $n = 6$ ) (Table 1; Figure 6).

#### 4.2.4. Type 4 CO<sub>2</sub> Fluid Inclusions

For type 4 CO<sub>2</sub> fluid inclusions, the first melting of the carbonic phase ( $T_{m(\text{CO}_2)}$ ) takes place either instantaneously at the pure CO<sub>2</sub> triple-point ( $-56.6$  °C) or within a narrow interval with lower melting temperatures of  $-59.1$  °C to  $-57.2$  °C (Table 1; Figure 6), indicating that the carbonic phase is near pure or probably comprise other minor quantities of gas species, such as CH<sub>4</sub> [50]. The homogenization of CO<sub>2</sub> ( $T_{h(\text{CO}_2)}$ ) into liquid takes place from  $21.2$  to  $29.3$  °C (mean  $25.8 \pm 3.1$  °C;  $1\sigma$ ;  $n = 5$ ), except for one inclusion, for which homogenization to vapor occurs at  $20.3$  °C (Table 1; Figure 6).

#### 4.3. Laser Raman Results

Laser Raman spectroscopy analysis was carried out for the typical fluid inclusions trapped in the quartz grains associated with the ore-forming event, so as to acquire the compositions of fluid inclusions, and the Laser Raman spectra obtained are shown in Figure 7. No other components were detected, except water in the liquid and vapor phases for the type 1 aqueous inclusions (Figure 7a,b). For the type 2 H<sub>2</sub>O–CO<sub>2</sub> (Figure 7c–e) and type 4 CO<sub>2</sub> inclusions (Figure 7f), some of the carbonic phases comprise nearly pure CO<sub>2</sub>, whereas others contain minor quantities of CH<sub>4</sub>.

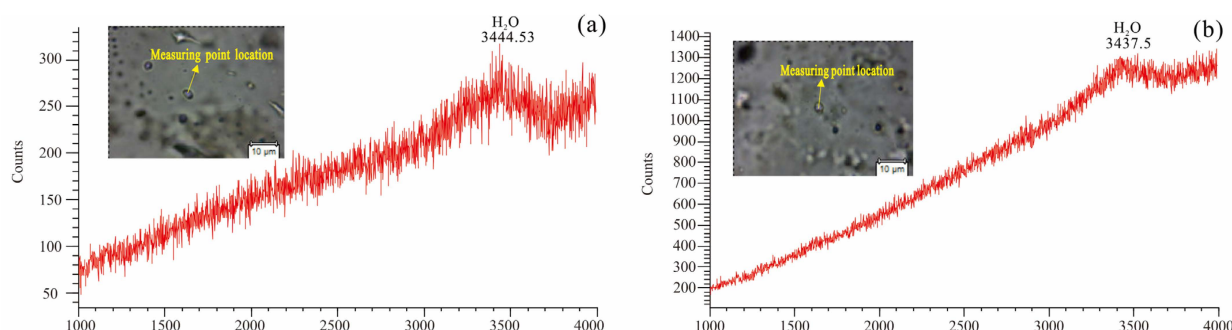
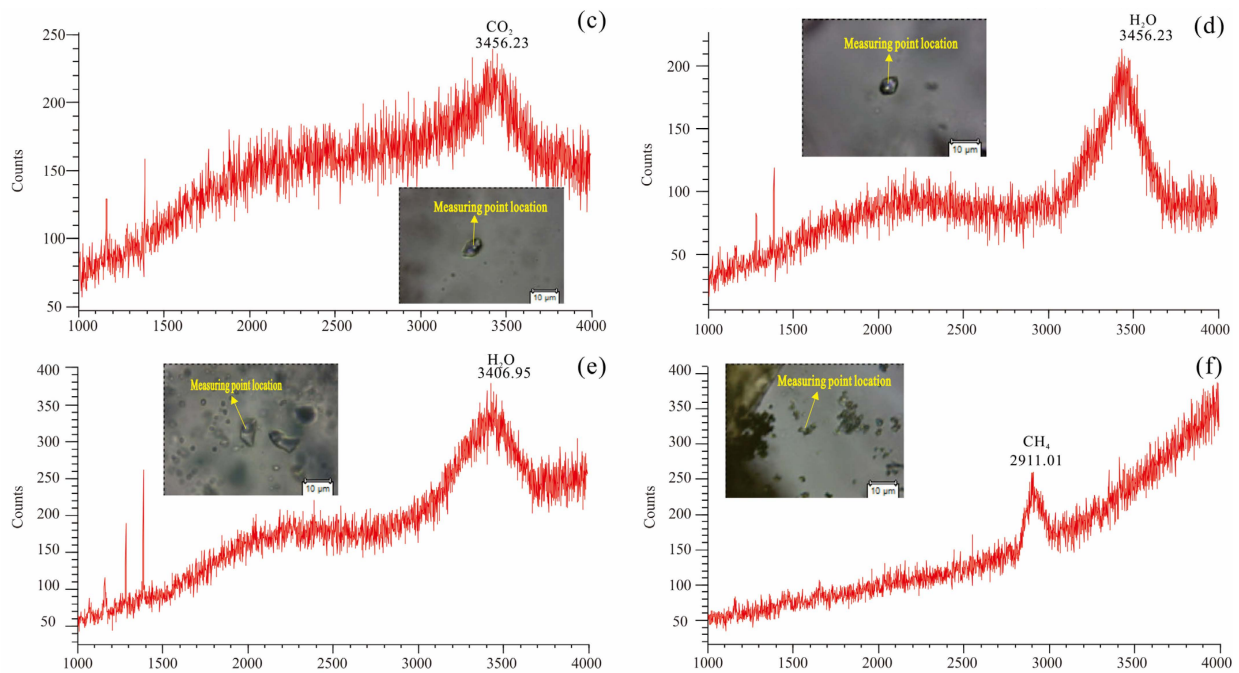


Figure 7. Cont.



**Figure 7.** Laser Raman spectra for fluid inclusions representative of the various types described from Xiawolong gold deposit. (a,b) Type 1 aqueous inclusions, (c–e) type 2 H<sub>2</sub>O–CO<sub>2</sub> inclusions, and (f) type 4 CO<sub>2</sub>.

#### 4.4. Composition and Density of Fluid Inclusions

Using the Bakker program [51] and MacFlincon software [52], the salinity, density, and composition of fluid inclusions were calculated according to the microthermometric data. In addition, the CH<sub>4</sub> content in the carbonic phase was calculated based on the V–X diagrams [53]. The corresponding results are displayed in Table 2.

##### 4.4.1. Salinity

Salinities in type 1 aqueous inclusions range from 0.18 to 17.00 wt.% equiv. NaCl (mean  $9.2 \pm 4.5$ ;  $1\sigma$ ;  $n = 76$ ; Table 2; Figure 8). Type 2 H<sub>2</sub>O–CO<sub>2</sub> inclusions contain 1.23–13.26 wt.% equiv. NaCl (mean  $7.8 \pm 3.1$ ;  $1\sigma$ ;  $n = 14$ ) (Table 2; Figure 8). The salinities of the type 3 daughter mineral-bearing inclusions are of 28.59–32.87 wt.% equiv. NaCl (mean  $30.6 \pm 1.4$ ;  $1\sigma$ ;  $n = 6$ ) (Table 2; Figure 8).

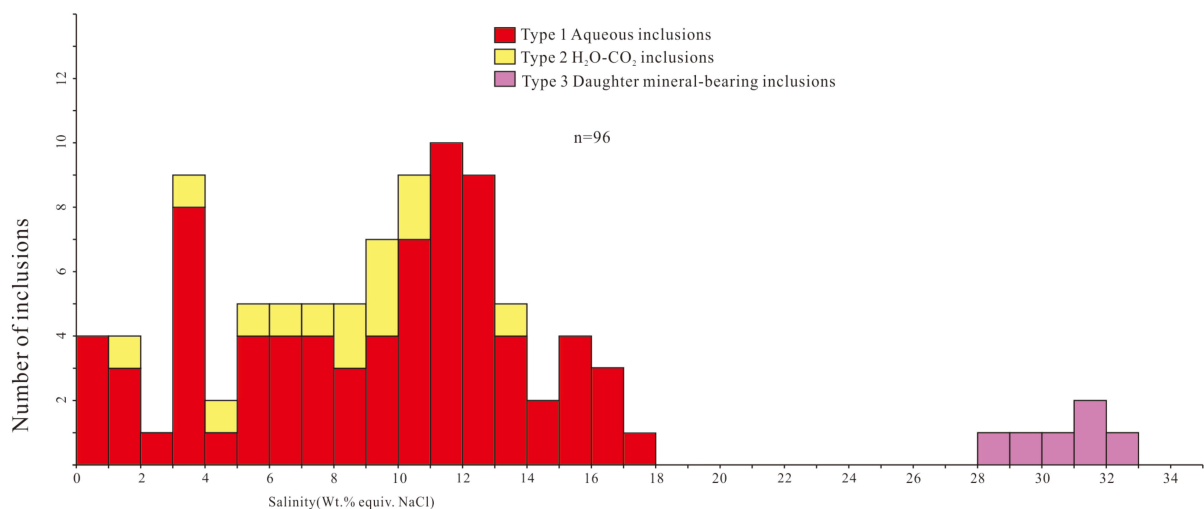


**Figure 8.** Frequency histograms of salinity (wt.% equiv. NaCl) of different types of fluid inclusions trapped in quartz.

**Table 2.** Composition of fluid inclusions trapped in quartz at the Xiawolong gold deposit. Note: data are given as mean, 1 $\sigma$  standard deviation, range, and number of measurements.

Ore Style	Fluid Inclusion Type	Eq. wt.% NaCl	Bulk XH <sub>2</sub> O	Bulk XNaCl	Bulk XCO <sub>2</sub> ± CH <sub>4</sub>	Carbonic XCO <sub>2</sub>	Carbonic XCH <sub>4</sub>	Bulk Density	Bulk Molar Volume
disseminated	Type 1 aqueous	0.35 to 17 (10.1 ± 4, n = 43)	1.05 to 2.14 (1.23 ± 0.22, n = 43)	0.0011 to 0.0594 (0.0341 ± 0.014, n = 43)	/	/	/	0.467 to 0.952 (0.831 ± 0.118, n = 43)	20.6 to 39.6 (23.9 ± 4.2, n = 43)
	Type 2 H <sub>2</sub> O-CO <sub>2</sub>	1.23 to 10.14 (6.41 ± 3.2, n = 7)	0.932 to 0.953 (0.941 ± 0.007, n = 7)	0.004 to 0.032 (0.020 ± 0.010, n = 7)	0.035 to 0.044 (0.038 ± 0.003, n = 7)	0.92 to 0.96 (0.94 ± 0.02, n = 7)	0.04 to 0.08 (0.06 ± 0.02, n = 7)	0.954 to 1.053 (1.010 ± 0.038, n = 7)	19.2 to 19.8 (19.5 ± 0.2, n = 7)
	Type 3 daughter mineral-bearing	28.6 to 32.9 (30.9 ± 1.8, n = 3)	1.12 to 1.15 (1.13 ± 0.02, n = 3)	0.11 to 0.13 (0.12 ± 0.01, n = 3)	/	/	/	0.866 to 0.896 (0.883 to 0.013, n = 3)	25.91 to 26.03 (25.96 ± 0.05, n = 3)
	Type 4 CO <sub>2</sub>	/	/	/	/	0.96 to 0.99 (0.97 ± 0.01, n = 3)	0.01 to 0.04 (0.03 ± 0.01, n = 3)	0.405 to 0.758 (0.537 ± 0.157, n = 3)	57.7 to 106.5 (86.6 ± 30.0, n = 3)
stockwork	Type 1 aqueous	0.18 to 16.35 (8.07 ± 4.92, n = 33)	1.02 to 1.82 (1.31 ± 0.23, n = 33)	0.0006 to 0.0575 (0.0270 ± 0.017, n = 33)	/	/	/	0.549 to 0.98 (0.785 ± 0.126, n = 33)	20.55 to 33.24 (24.91 ± 3.72, n = 33)
	Type 2 H <sub>2</sub> O-CO <sub>2</sub>	5.77 to 13.26 (9.1 ± 2.2, n = 7)	0.93 to 0.95 (0.94 ± 0.006, n = 7)	0.018 to 0.044 (0.029 ± 0.008, n = 7)	0.031 to 0.036 (0.034 ± 0.001, n = 7)	0.91 to 0.97 (0.95 ± 0.02, n = 7)	0.03 to 0.09 (0.05 ± 0.02, n = 7)	0.998 to 1.042 (1.019 ± 0.015, n = 7)	19.3 to 19.6 (19.5 ± 0.1, n = 7)
	Type 3 daughter mineral-bearing	29.3 to 31.5 (30.3 ± 0.9, n = 3)	1.13 to 1.16 (1.14 ± 0.01, n = 3)	0.113 to 0.124 (0.018 ± 0.005, n = 3)	/	/	/	0.865 to 0.887 (0.879 ± 0.010, n = 3)	25.8 to 26.1 (25.9 ± 0.2, n = 3)
	Type 4 CO <sub>2</sub>	/	/	/	/	0.95 to 0.99 (0.98 ± 0.02, n = 3)	0.01 to 0.05 (0.02 ± 0.02, n = 3)	0.438 to 0.747 (0.629 ± 0.136, n = 3)	58.5 to 97.4 (72.7 ± 17.5, n = 3)

#### 4.4.2. Carbonic Phase Composition

For type 2 H<sub>2</sub>O–CO<sub>2</sub> inclusions, the results of Laser Raman analysis (Figure 7) and the carbonic phase melting temperatures ( $T_{m(\text{CO}_2)}$ ) reveal temperatures 3.0 °C lower than the CO<sub>2</sub> triple-point (−56.6 °C) (Table 1; Figure 6), indicating that the CH<sub>4</sub> existed in the carbonic phase. The XCH<sub>4</sub> was found to be 3–9 mol% (mean  $6 \pm 3$  mol%; 1 $\sigma$ ; n = 12; Table 2) according to  $T_{h(\text{CO}_2)}$  and  $T_{m(\text{CO}_2)}$  on the basis of the V–X diagrams [53].

#### 4.4.3. Bulk Composition and Density

The densities of type 1 aqueous inclusions were calculated to be between 0.467 and 0.98 g/cm<sup>3</sup>. Type 2 H<sub>2</sub>O–CO<sub>2</sub> inclusions consist of ca. 90 mol% H<sub>2</sub>O and CO<sub>2</sub>, varying from 3.1 to 4.4 mol% with an average value of  $3.6 \pm 0.3$  mol% (1 $\sigma$ ; n = 14; Table 2). The bulk densities of type 2 H<sub>2</sub>O–CO<sub>2</sub> inclusions are 0.954–1.053 g/cm<sup>3</sup> (mean  $1.015 \pm 0.030$  g/cm<sup>3</sup>; 1 $\sigma$ ; n = 14). The densities of type 3 daughter mineral-bearing inclusions range from 0.865 to 0.896 g/cm<sup>3</sup>. For type 4 CO<sub>2</sub> inclusions, the bulk densities are 0.405 to 0.758 g/cm<sup>3</sup> (mean  $0.583 \pm 0.154$  g/cm<sup>3</sup>; 1 $\sigma$ ; n = 6; Table 2), with a constant XCO<sub>2</sub> (0.952 to 0.990).

### 5. Isotope Geochemistry

#### 5.1. $\delta^{18}\text{O}$ and $\delta\text{D}$ of Quartz and Ore-Forming Fluids

The D–O isotope data for the hydrothermal quartz selected from eight gold-bearing disseminated and stockwork-style fine-grained granitic ores are given in Table 3. The measured  $\delta^{18}\text{O}$  values of hydrothermal quartz ( $\delta^{18}\text{O}_{\text{quartz}}$ ) range from 6.8 to 9.3‰ (mainly 8.4 to 8.7‰), with an average value of 8.4‰ (Table 3). The  $\delta\text{D}$  values of fluid inclusions in hydrothermal quartz ( $\delta\text{D}_{\text{quartz}}$ ) range from −97.1 to −77.4‰, with an average value of −87.4‰ (Table 3).

**Table 3.** The D–O isotopic composition of quartz in the Xiawolong gold deposit.

Ore Style	Sample	$\delta\text{D}_{\text{water}}$ (‰)	$\delta^{18}\text{O}_{\text{quartz}}$ (‰)	$\delta^{18}\text{O}_{\text{water}}$ (‰)	T (°C)
stockwork-style ores	XWL-g9	−85.0	9.3	5.9	431
	XWL-g11	−77.4	8.4	5.0	431
	XWL-g16	−81.5	8.7	5.3	431
	XWL16D001B2	−90.3	8.6	5.2	431
Disseminated ores	TZ2ZK3-5	−92.7	8.5	5.1	431
	XTS-37~41				
	2ZK317	−86.6	6.8	3.4	431
	TS②ZK2-31	−89.1	8.5	5.1	431
	XTS-21~25				
	TS②ZK2-43	−97.1	8.5	5.1	431

The  $\delta^{18}\text{O}_{\text{water}}$ , i.e., the  $\delta^{18}\text{O}$  value of hydrothermal waters in equilibrium with hydrothermal quartz, is obtained based on the isotopic fraction equation of  $\delta^{18}\text{O}_{\text{water}} = \delta^{18}\text{O}_{\text{quartz}} - 3.38 \times 10^6 T^{-2} + 3.4$  [54], where T is the oxygen isotope equilibrium temperature between the hydrothermal quartz and water, which is estimated to be 431 °C based on the homogenization temperatures obtained from the type 3 daughter mineral-bearing inclusions (Table 1). Accordingly, the calculated  $\delta^{18}\text{O}_{\text{water}}$  values vary from 3.4 to 5.9‰ (mainly 5.0 to 5.9‰), with an average value of 5.1‰ (Table 3).

#### 5.2. $\delta^{34}\text{S}$ Isotope and Pb Compositions of Pyrite

The hydrothermal pyrites picked from 13 gold-bearing disseminated and stockwork-style fine grained granitic ores were used to carry out  $\delta^{34}\text{S}$  and Pb isotope analyses (Table 4). The results show that the  $\delta^{34}\text{SCDT}$  values of the hydrothermal pyrites possess a relatively narrow range of 4.5 to 9.3‰ (mainly 6.2 to 8.1‰), with an average value of 6.7‰. Similarly, the Pb isotopic ratios also show narrow ranges, with  $^{206}\text{Pb}/^{204}\text{Pb}$  ratios of 17.000 to 17.792,  $^{207}\text{Pb}/^{204}\text{Pb}$  ratios of 15.415 to 15.520, and  $^{208}\text{Pb}/^{204}\text{Pb}$  ratios of 37.176 to 37.870.

**Table 4.** Sulfur isotopic compositions and lead isotopic ratios of pyrite in the Xiawolong gold deposit.

Ore Style	Sample	$\delta^{34}\text{S}_{\text{CDT}}$ (‰)	$^{208}\text{Pb}/^{204}\text{Pb}$	$^{207}\text{Pb}/^{204}\text{Pb}$	$^{206}\text{Pb}/^{204}\text{Pb}$
Stockwork ores	XWL-g1	6.6	37.369	15.436	17.247
	XWL-g3	6.9	37.870	15.504	17.792
	XWL-g9	6.1	37.432	15.444	17.193
	XWL-g10	7.6	37.490	15.468	17.481
	XWL-g11	7.1	37.472	15.459	17.526
	XWL-g12	7	37.498	15.467	17.500
	XWL-g16	8.1	37.453	15.459	17.432
Disseminated ores	TZ2ZK3-5	6.6	37.619	15.480	17.297
	XTS-37~41				
	TZ2ZK3-4	6	37.294	15.415	17.000
	XTS-32~36				
	2ZK317	4.5	37.745	15.520	17.586
	TS②ZK2-31	6.2	37.176	15.432	17.040
	TS-21~25				
	TS②ZK2-43	5.2	37.519	15.479	17.390
	TS7ZK1-8				
XTS-42~45	9.3	37.436	15.458	17.240	

## 6. Discussion

### 6.1. Source of Ore-Forming Fluids

The  $\delta^{18}\text{O}$  values of hydrothermal quartzes have a narrow range of 6.8 to 9.3‰ (typically 8.4 to 8.7‰) (Table 3), suggesting that these hydrothermal quartzes are formed during the same stage. Figure 9 shows that the value of  $\delta^{18}\text{O}_{\text{water}}$  nearly lies within the field of primary magmatic water, indicating the origin of magmatic water [55]. The  $\delta\text{D}_{\text{water}}$  values are  $-97.1$  to  $-77.4$ ‰, being slightly lower than those of the primary magmatic water and overlapping with the lower end of the Sanfoshan Granite magmatic waters (Figure 9), which likely results from the early degassing process in an open magma system [56–60].

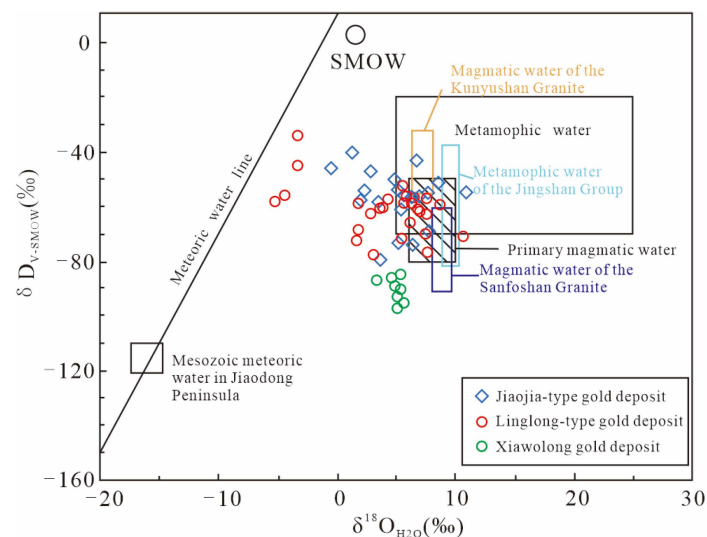


**Figure 9.** Calculated  $\delta\text{D}$  and  $\delta^{18}\text{O}$  values of ore-forming fluids in the Xiawolong gold deposit. Data for the areas of magmatic water of the Kunyushan granite, magmatic water of the Sanfoshan granite, metamorphic water of the Jinshan Group, and the “Jiaojia-type” and “Linglong-type” gold deposits are from [20,61] and references therein. Adapted with permission from Ref. [20]. 2017, Elsevier and Ref. [61]. 2014, *Acta Petrol. Sin.*

In addition, none of the D-O isotopic data of ore-forming fluids in the Xiawolong gold deposit fall within the values for magmatic waters of the Mesozoic Kunyushan, or the metamorphic water of the Jingshan Group (Figure 9), indicating that it is impossible

that the ore-forming fluids were derived from these rocks. Furthermore, the  $\delta^{18}\text{O}$  and  $\delta\text{D}$  compositions possess a narrow region, without an obvious linear decreasing or increasing trend, as shown in Figure 9, which may indicate that during the ore-forming stage, no water–rock interaction and/or mixing with another source fluid occurred. This is consistent with the fact that no hydrothermal alteration, fault, or fracture developed in the Xiawolong gold deposit. Therefore, it is logical to conclude that the ore-forming fluid in the Xiawolong gold deposit is likely of a magmatic source.

The type 1 aqueous inclusions have a eutectic temperature of 58.4 to  $-51.2\text{ }^{\circ}\text{C}$ , indicating the existence of  $\text{CaCl}_2$  in the fluid [62]. The identification of daughter minerals, such as sylvite and  $\text{CO}_2$  in fluid inclusions, proves that  $\text{KCl}$  and  $\text{CO}_2$  are important components. As a result, the ore-forming fluid of Xiawolong gold deposit should be ascribed to the  $\text{NaCl-CaCl}_2\text{-KCl-CO}_2\text{-H}_2\text{O}$  system.

Middle-high temperature mineral assemblages, such as molybdenite and magnetite, are usually associated with gold-bearing pyrite in disseminated and stockwork-style fine-grained granitic ores in the Xiawolong gold deposit. Furthermore, the type 3 daughter mineral-bearing inclusions are represented by high temperature ( $416$  to  $439\text{ }^{\circ}\text{C}$ ) and high salinity ( $32.87$  to  $28.59\text{ wt.}\%$   $\text{NaCl}$  equiv.), whereas the type 1 aqueous and type 2  $\text{H}_2\text{O-CO}_2$  inclusions show the relatively lower temperature and salinity, being  $201$  to  $480\text{ }^{\circ}\text{C}$  and  $0.18$  to  $17.00\text{ wt.}\%$   $\text{NaCl}$  equiv. for the type 1 aqueous inclusions, and  $218$  to  $385\text{ }^{\circ}\text{C}$  and  $1.23$  to  $13.26\text{ wt.}\%$   $\text{NaCl}$  equiv. for the type 2  $\text{H}_2\text{O-CO}_2$  inclusions (Figure 10). In addition, it can be seen that the type 1 aqueous, type 2  $\text{H}_2\text{O-CO}_2$ , and type 3 daughter mineral-bearing inclusions coexisted in the same view field. Therefore, it is logical to infer that it is impossible for these inclusions to have been captured from a homogeneous fluid system, whereas the similar homogenization temperatures obtained suggest fluid immiscibility, resulting from extensive fluid boiling. The fluid immiscibility changes the chemical and physical properties of the ore-forming fluid system, which is beneficial to the deposition of pyrite, magnetite, molybdenite, and other sulfide minerals.

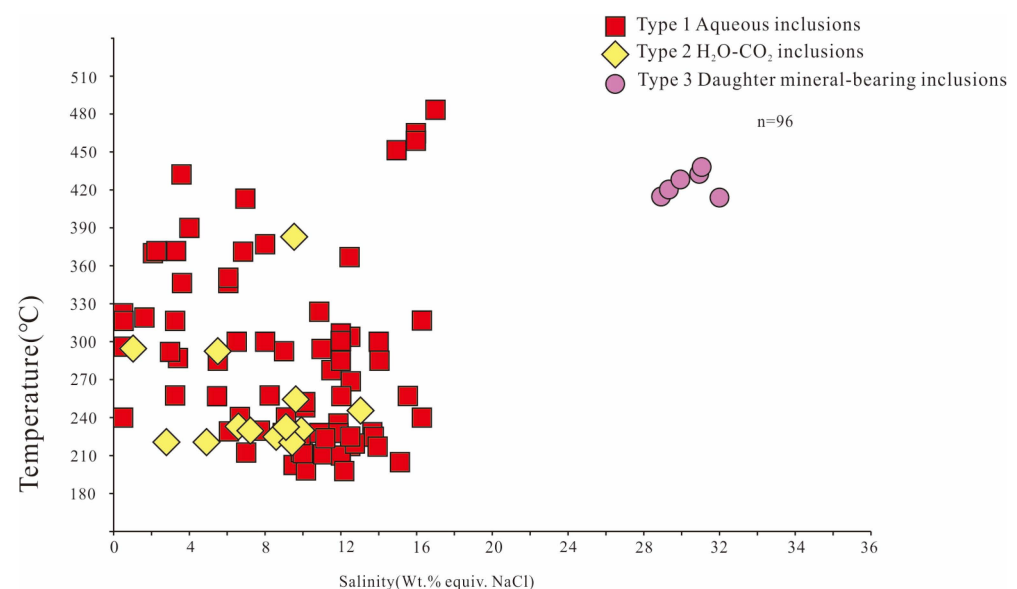


**Figure 10.** Temperatures ( $^{\circ}\text{C}$ ) of total homogenization ( $T_{\text{h}(\text{tot})}$ ) versus salinity (wt.% equiv.  $\text{NaCl}$ ) for different types of fluid inclusions trapped in quartz in the Xiawolong gold deposit.

## 6.2. Ore-Forming Material Sources

The  $\delta^{34}\text{S}$  values of hydrothermal pyrite in the gold-bearing disseminated and stockwork-style fine-grained granitic ores possess a narrow range, from  $4.5$  to  $9.3\text{ }_{\text{‰}}$  (mainly  $6.2$  to  $8.1\text{ }_{\text{‰}}$ ) (Figure 11a), with an average value of  $6.7\text{ }_{\text{‰}}$ , indicating that they originated from the same source. All values are at the top part of the spectrum of the representative range of orogenic gold deposits [63,64], and also within the ranges of the Mesozoic Kunyushan

granitoids (Figure 11b). Therefore, the  $\delta^{34}\text{S}$  value in the Xiawolong gold deposit could be derived from the Mesozoic Kunyushan granitoids.

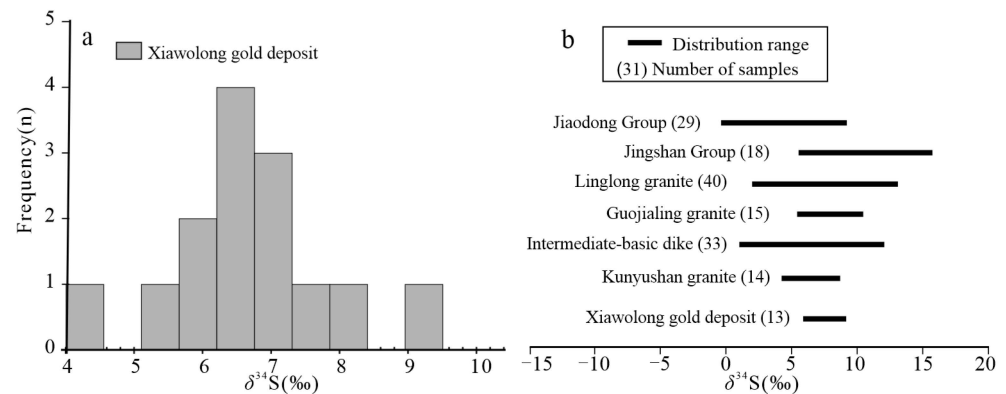


**Figure 11.** (a) Histograms of  $\delta^{34}\text{S}$  values of hydrothermal pyrites from the Xiawolong gold deposit. (b) Comparison of sulfur isotopic compositions in Xiawolong and related major geologic bodies. The ranges of major geologic bodies are from [65]. Adapted with permission from Ref. [65]. 2014, *Acta Petrol. Sin.*

The Pb isotopic compositions of the hydrothermal pyrite in the gold-bearing disseminated and stockwork-style fine-grained granitic ores possess a narrow range and overlap with those of the metamorphic rocks of the Paleoproterozoic Jingshan group (Figure 12). Moreover, they overlap with the field of Mesozoic Kunyushan granitoid, which is the main host rock of the Xiawolong gold deposit. Thus, the Pb isotopic compositions of pyrite can be considered to mainly come from the host rocks. In addition, the Pb isotopic compositions of these pyrites span the lower crust and orogenic line (Figure 12), indicating that they are likely from the lower crust and are related to the orogenic lead reservoir.

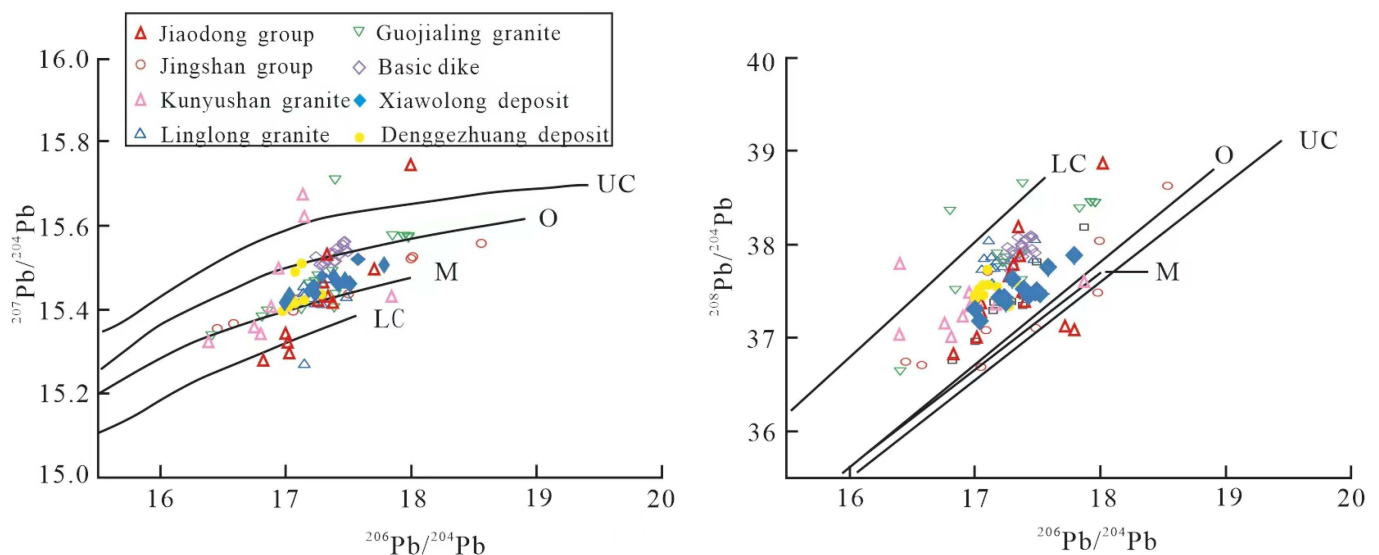


**Figure 12.** Pb isotopic compositions of pyrite in the Xiawolong gold deposit. The evolution lines for major geological units are from Zartman and Haines [66]. Adapted with permission from Ref. [66]. 1988, Elsevier. UC, upper crust; O, orogen; M, mantle; LC, lower crust.

### 6.3. Gold Precipitation Mechanism

In the Early Cretaceous, the Jiaodong Peninsula underwent lithospheric extension and thinning, which led to strong magmatic activity [42]. During the process of granitic magma invading along the structure, the crystallization differentiation of the magmatic system itself probably resulted in the late-stage magmatic hydrothermal fluid being rich

in Be-Li-Nb-Ta-Sn-Bi-W-Mo-Cu-Zn-U-Au [25–28]. With regard to the late stage of granitic magmatic crystallization, the fluid is dominantly sourced from magma degassing and fluid exsolution, which is represented by both high salinity and temperature. When the fluid migrates upward and suffers structural fracture, the release of fluid pressure and the boiling of fluid occurred suddenly, which resulted in the fluid immiscibility indicated by the coexistence of type 1 aqueous, type 2 H<sub>2</sub>O–CO<sub>2</sub>, and type 3 daughter mineral-bearing fluid inclusions in the same view field. The fluid immiscibility makes an important contribution to the precipitation of molybdenite, magnetite, pyrite, and other sulfides.

The Au of the Xiawolong deposit develops mostly in the form of pyrite. Previous studies suggested that Au can migrate in several complex forms through the ore-forming fluid system. The main theories on the mechanism of Au precipitation, forming complexes in hydrothermal solution, are as follows: natural cooling [67–69], mixing of different fluids [8,67,70–73], fluid boiling or immiscibility [74–79], a change in pH or oxygen fugacity and the water–rock reaction [80–83], and pressure decrease [81]. The Au precipitation in the Xiawolong deposit is mostly concentrated in the fine-grained granite. The fluid immiscibility changes the chemical and physical properties of the ore-forming fluid system [84], resulting in the deposition of pyrite, magnetite, molybdenite, and other sulfide minerals.

#### 6.4. Comparison with other Gold Deposits in the Jiaodong Peninsula

As mentioned above, the “Jiaojia-type”, characterized by the Xincheng, Jiaojia, Luoshan, and Taishang gold deposits (Figure 1), and the “Linglong-type”, characterized by the Linglong, Fushan, and Wang’ershan gold deposits (Figure 1), are the two types of gold mineralization in the Jiaodong Peninsula. Although the “Jiaojia-type” is composed of stockwork and disseminated pyrite–sericite–quartz-altered ores hosted within the first-order regional faults, and the “Linglong-type” is represented by gold-bearing quartz veins hosted in the lower-order NNE- to NE-trending faults, they both have similar ore-forming ages, mineral paragenesis, and alteration assemblages [1,61]. They are characterized by middle-low temperature ore mineral assemblages, including pyrite, chalcopyrite, galena, and sphalerite [20]. Three types of fluid inclusions associated with gold mineralization are H<sub>2</sub>O–CO<sub>2</sub>–NaCl, aqueous, and CO<sub>2</sub> fluid inclusions [1]. The ore-forming fluid is represented by medium-high homogenization temperatures of 211 to 393 °C, significant CO<sub>2</sub> (ca.15% mol), minor amounts of CH<sub>4</sub> (≤18% in the carbonic phase), and low salinity (≤11.2 wt.% NaCl eq.) [1,20]. Most of the hydrogen–oxygen isotopic data of both the “Jiaojia-type” and the “Linglong-type” gold ore deposits are concentrated within the range of –80‰ to –33‰ for δD and –5‰ to 11‰ for δ<sup>18</sup>O (Figure 9), suggesting that the ore-forming fluids possess a metamorphic source together with the mixing of meteoric water [20,61]. The δ<sup>34</sup>S values of hydrothermal pyrite have a narrow range, from 4.5‰ to 8.0‰, and are within the very broad range of the majority of lode gold deposits [63,64]. In general, both the “Jiaojia-type” and “Linglong-type” of gold mineralization are formed in large-scale unified events, in terms of the consistent ore-forming process, mechanism of gold deposition and timing of gold mineralization, are considered to be orogenic gold deposits [1–3].

However, the Xiawolong gold deposit is hosted in late Early Cretaceous fine-grained granite, which is generally fresh and non-deformed. All of the gold orebodies are represented by the stockwork-style and disseminated ores developed in the fresh fine-grained granite dikes. No hydrothermal alteration surrounded the orebodies. Middle-high temperature mineral assemblages, such as molybdenite and magnetite, are usually associated with gold-bearing pyrite. The fluid inclusions can be divided into four types: type 1 aqueous, type 2 H<sub>2</sub>O–CO<sub>2</sub>, type 3 daughter mineral-bearing, and type 4 CO<sub>2</sub> fluid inclusions. The ore-forming fluid of the Xiawolong gold deposit has a magmatic source and is mainly a NaCl–CaCl<sub>2</sub>–KCl–H<sub>2</sub>O system with high temperature (416 to 446 °C) and high salinity (32.87 to 28.59 wt.% NaCl equiv.). The δ<sup>34</sup>S value is derived from that of the Mesozoic Kunyushan granitoids. The Pb isotopic compositions of pyrite show that it is likely that the Mesozoic Kunyushan granitoids are the main source of Pb.

In view of the distinct stable isotope compositions and ore-forming fluid systems, together with the discordant wall-rock alteration assemblages, structural systems, nature of orebodies, and gold occurrence conditions, it is concluded that the gold mineralization in the Xiawolong deposit, associated with the fine-grained granite, is different from the “Jiaojia-type” and “Linglong-type” gold deposits in the Jiaodong Peninsula.

### 6.5. Implications for Intrusion-Related Gold Systems

As mentioned above, the gold orebodies in the Xiawolong deposit occur in the fresh fine-grained granite dikes, and K-feldspar crystals are observed on the edge of some quartz veins. These observations, and the presence of K-feldspar crystals hosted in pyrite (Figure 4f), indicate the transition from the final stage of magmatism towards the formation of orebodies with the presence of other sulfides (Figure 4h–k), suggesting that the mineralization paragenesis is intimately related to the magmatic stage [85]. These findings are comparable to similar features described in the Passa Três gold deposit (southern Brazil), where aplitic dikes occur close to or along gold-bearing quartz veins [85]. It should be noted that these features usually occur within the roof zone of the granitic system [86], such as the syenite-associated gold deposits in the Abitibi greenstone belt in Canada [87], the Porgera gold deposit in the highlands of Papua New Guinea [88], or the Timbarra gold deposit in Australia [89].

In intrusion-related environments, the most favorable areas for the formation of gold deposits are apical portions of small intrusions [90], such as the Fort Knox deposit [89]. According to [91], the shallow intrusion-related gold deposits (<5 km) usually have fluid inclusions with high temperatures and high salinities, as well as low-salinity CO<sub>2</sub> fluid inclusions, which are characteristic for the Xiawolong deposit. Furthermore, the D-O isotopes indicate a magmatic water origin for the ore-forming fluid in the Xiawolong deposit. Therefore, it is logical to conclude that for the Xiawolong gold deposit, the ore-forming process is the result of the fluid release that can occur during the transition from magmatic to hydrothermal stages.

## 7. Conclusions

(1) The Xiawolong gold deposit is hosted in late Early Cretaceous fine-grained granite and is represented by stockwork-style and disseminated ores, with high-temperature mineral assemblages, such as molybdenite and magnetite, associated with the gold-bearing pyrite.

(2) Four types of primary fluid inclusions in the Xiawolong gold deposits were identified: type 1 aqueous, type 2 H<sub>2</sub>O–CO<sub>2</sub>, type 3 daughter mineral-bearing, and type 4 CO<sub>2</sub> fluid inclusions (in order of the decreasing abundance of fluid inclusions). The ore-forming fluid is of a NaCl–CaCl<sub>2</sub>–KCl–H<sub>2</sub>O system, represented by both high temperature (416 to 446 °C) and salinity (32.87 to 28.59 wt.% NaCl equiv.).

(3) The D-O isotopes indicate a magmatic water origin for the ore-forming fluid, and magma degassing resulting in a decrease in fluid δD. The S isotope indicates that the sulfur is from the Mesozoic Kunyushan granitoids. The Pb isotopic compositions of pyrite show that it is likely that the Mesozoic Kunyushan granitoids are the main source of Pb.

(4) The fluid immiscibility, rather the wall-rock sulfidation and fluid mixing, causes changes in the chemical and physical properties of the ore-forming fluid system, resulting in the deposition of pyrite, magnetite, molybdenite, and other sulfide minerals.

(5) The Xiawolong gold deposit is a magmatic hydrothermal deposit having a genetic relation to the fine-grained granite, unlike the “Jiaojia-type” and “Linglong-type” gold deposits in the Jiaodong Peninsula.

**Author Contributions:** Conceptualization, J.L. and Z.W.; Data curation, J.L. and Z.W.; Formal analysis, J.L., Z.D., M.Z. and M.W.; Funding acquisition, Z.W.; Investigation, J.L., Z.W., Z.D., R.Z., M.Z., Z.B. and F.T.; Methodology, J.L.; Project administration, Z.W.; Resources, J.L., Z.W., Z.D. and R.Z.; Software, J.L., Z.W., R.Z. and M.W.; Supervision, Z.W.; Validation, J.L.; Visualization, J.L. and

Z.W.; Writing—original draft, J.L., Z.W. and Z.D.; Writing—review and editing, J.L. and Z.W. All authors have read and agreed to the published version of the manuscript.

**Funding:** This study was financially supported by the National Natural Science Foundation of China (Grant No. 41772061), and the Scientific and technological research project of Shandong Geology and Mineral Bureau (Grant No. KY201405).

**Institutional Review Board Statement:** Not applicable.

**Informed Consent Statement:** Not applicable.

**Data Availability Statement:** The datasets presented in this study can be obtained upon request to the corresponding author.

**Acknowledgments:** Constructive comments from the editor Jim Zhang, and the revisions from two anonymous reviewer greatly improved the manuscript of this paper. We thank the team members at China University of Geosciences (Beijing) for their field support and comments.

**Conflicts of Interest:** The authors declare no conflict of interest.

## References

1. Wang, Z.L.; Yang, L.Q.; Guo, L.N.; Marsh, E.; Wang, J.P.; Liu, Y.; Zhang, C.; Li, R.H.; Zhang, L.; Zheng, X.L.; et al. Fluid immiscibility and gold deposition in the Xincheng deposit, Jiaodong Peninsula, China: A fluid inclusion study. *Ore Geol. Rev.* **2015**, *65*, 701–717. [[CrossRef](#)]
2. Song, M.C.; Li, S.Z.; Santosh, M.; Zhao, S.; Yu, S.; Yi, P.H.; Cui, S.X.; Lv, G.X.; Xu, J.X.; Song, Y.X.; et al. Types, characteristics and metallogenesis of gold deposits in the Jiaodong Peninsula, Eastern North China Craton. *Ore Geol. Rev.* **2015**, *65*, 612–625. [[CrossRef](#)]
3. Goldfarb, R.J.; Santosh, M. The dilemma of the Jiaodong gold deposits: Are they unique? *Geosci. Front.* **2014**, *5*, 139–153. [[CrossRef](#)]
4. Zhu, R.X.; Fan, H.R.; Li, J.W.; Meng, Q.R.; Li, S.R. Decratonic gold deposits. *Sci. China Ser. D Earth Sci.* **2015**, *58*, 1523–1537. [[CrossRef](#)]
5. Yang, K.F.; Jiang, P.; Fan, H.R.; Zuo, Y.B.; Yang, Y.H. Tectonic transition from a compressional to extensional metallogenic environment at similar to 120 Ma revealed in the Hushan gold deposit, Jiaodong, North China craton. *J. Asian Earth Sci.* **2018**, *160*, 408–425. [[CrossRef](#)]
6. Li, J.W.; Bi, S.J.; Selby, D.; Chen, L.; Vasconcelos, P.; Thiede, D.; Zhou, M.F.; Zhao, X.F.; Li, Z.K.; Qiu, H.N. Giant Mesozoic gold provinces related to the destruction of the North China craton. *Earth Planet Sci. Lett.* **2012**, *349–350*, 26–37. [[CrossRef](#)]
7. Mao, J.W.; Li, H.M.; Wang, Y.T.; Zhang, C.Q.; Wang, R.T. The relationship between mantle-derived fluid and gold ore-formation in the eastern Shandong Peninsula: Evidences from D-O-C-S isotopes. *Acta Geol. Sin.* **2005**, *79*, 839–857, (In Chinese with English abstract). [[CrossRef](#)]
8. Wang, X.D.; Ni, P.; Jiang, S.Y.; Zhao, K.D.; Wang, T.G. Origin of ore-forming fluid in the Piaotang tungsten deposit in Jiangxi Province: Evidence from helium and argon isotopes. *Chin. Sci. Bull.* **2010**, *55*, 628–634. [[CrossRef](#)]
9. Ying, H.L. Deposit and Mineral Geochemistry and Ore Genesis of Jinqingding and Denggezhuang Gold Deposits, Jiaodong Peninsula. Ph.D. Thesis, Institute of Geology, Chinese Academy of Sciences, Beijing, China, 1993; p. 119. (In Chinese).
10. Wang, Z.Y.; Lv, G.X.; Zhang, X.Y.; Han, X.; Zhang, Y.C.; Fan, X.; Huo, Q.L.; Xu, Y.Q. Rb-Sr isotopic geochronology and geological implications of Dongfeng gold deposit in Jiaodong area. *Earth Sci. Res. J.* **2016**, *20*, 1–17. [[CrossRef](#)]
11. Zhang, L.; Weinberg, R.F.; Yang, L.Q.; Groves, D.I.; Sai, S.X.; Matchan, E.; Phillips, D.; Kohn, B.P.; Miggins, D.P.; Liu, Y.; et al. Mesozoic Orogenic Gold Mineralization in the Jiaodong Peninsula, China: A Focused Event at  $120 \pm 2$  Ma during Cooling of Pregold Granite Intrusions. *Econ. Geol.* **2020**, *115*, 415–441. [[CrossRef](#)]
12. Liu, S.N. On the model of space location of ore bodies and its mechanism of Linglong-type gold ore deposit. *Earth Sci.* **1984**, *4*, 47–56, (In Chinese with English abstract).
13. Lu, H.Z.; Archambault, G.; Li, Y.; Wei, J. Structural geochemistry of gold mineralization in the Linglong-Jiaojia district, Shandong Province. *Chin. J. Geochem.* **2007**, *26*, 215–234, (In Chinese with English abstract). [[CrossRef](#)]
14. Qiu, Y.M.; Groves, D.I.; McNaughton, N.J.; Wang, L.G.; Zhou, T.H. Nature, age and tectonic setting of granitoid-hosted, orogenic gold deposits of the Jiaodong Peninsula, eastern North China Craton, China. *Miner. Depos.* **2002**, *37*, 283–305. [[CrossRef](#)]
15. Li, X.C.; Fan, H.R.; Santosh, M.; Hu, F.F.; Yang, K.F.; Lan, T.G. Hydrothermal alteration associated with Mesozoic granite-hosted gold mineralization at the Sanshandao deposit, Jiaodong Gold Province, China. *Ore Geol. Rev.* **2013**, *53*, 403–421. [[CrossRef](#)]
16. Guo, P.; Santosh, M.; Li, S.R. Geodynamics of gold metallogeny in the Shandong Province, NE China: An integrated geological, geophysical and geochemical perspective. *Gondwana Res.* **2013**, *24*, 1172–1202. [[CrossRef](#)]
17. Groves, D.I.; Santosh, M. The giant Jiaodong gold province: The key to a unified model for orogenic gold deposits? *Geosci. Front.* **2016**, *7*, 409–418. [[CrossRef](#)]
18. Yang, F.; Santosh, M.; Tang, L. Extensive crustal melting during craton destruction: Evidence from the Mesozoic magmatic suite of Junan, eastern North China Craton. *J. Asian Earth Sci.* **2017**, *157*, 119–140. [[CrossRef](#)]

19. Zhang, X.O.; Cawood, P.A.; Wilde, S.A.; Liu, R.Q.; Song, H.L.; Li, W. Snee LW Geology and timing of mineralization at the Cangshang gold deposit, north-western Jiaodong Peninsula, China. *Miner. Depos.* **2003**, *38*, 141–153. [[CrossRef](#)]
20. Guo, L.N.; Goldfarb, R.J.; Wang, Z.L.; Li, R.H.; Chen, B.H.; Li, J.L. A comparison of Jiaojia- and Linglong-type gold deposit ore-forming fluids: Do they differ? *Ore Geol. Rev.* **2017**, *88*, 511–533. [[CrossRef](#)]
21. Zhou, T.; Goldfarb, R.J.; Phillips, G.N. Tectonics and distribution of gold deposits in China. *Miner. Depos.* **2002**, *37*, 249–282. [[CrossRef](#)]
22. Fan, H.R.; Zhai, M.G.; Xie, Y.H.; Yang, J.H. Ore-forming fluids associated with granite-hosted gold mineralization at the Sanshandao deposit, Jiaodong gold province, China. *Miner. Depos.* **2003**, *38*, 739–750. [[CrossRef](#)]
23. Li, S.R.; Santosh, M. Geodynamics of heterogeneous gold mineralization in the North China Craton and its relationship to lithospheric destruction. *Gondwana Res.* **2017**, *50*, 267–292. [[CrossRef](#)]
24. Lv, J.Y.; Wang, F.J.; Hu, B.Q.; Wang, X.R.; Zhang, P.; Teng, F. Geological Characteristics and Ore Prospecting Direction of A New Type Gold Deposit Hosted In Fine—Grained Granite in Kunyushan Area in Shandong Province—Setting Xiawolong Gold Deposit as an Example. *Shandong Land Resour.* **2017**, *33*, 1–6.
25. Antunes, I.M.H.R.; Neiva, A.M.R.; Ramos, J.M.F.; Silva, P.B.; Silva, M.M.V.G.; Corfu, F. Petrogenetic links between lepidolite-subtype aplite-pegmatite, aplite veins and associated granites at Segura (central Portugal). *Chem. Erde.* **2013**, *73*, 323–341. [[CrossRef](#)]
26. Li, J.; Zhang, W.L.; Gao, M.Q.; Dang, F.P. Zircon LA-ICP-MS U-Pb isotopic dating age of fine-grained granite in Lujing uranium field and its geological significance. *Miner. Resour. Geol.* **2019**, *33*, 489–495, 501, (In Chinese with English abstract).
27. Allen, F.G.; John, M.B.; Drew, S.C.; Kjell, L. Aplite diking and infiltration: A differentiation mechanism restricted to plutonic rocks. *Miner. Petrol.* **2020**, *175*, 37. [[CrossRef](#)]
28. Zhang, X.F.; Li, W.C.; Yang, Z.; Gao, X.; Zhu, J.; Liu, W.D. Implications of aplite dykes for mineralization in the Late Cretaceous vein-type Xiuwacu W-Mo deposit in the southern Yidun Terrane, SE Tibetan Plateau. *J. Asian Earth Sci.* **2020**, *204*, 104555. [[CrossRef](#)]
29. Harald, G.D. Pegmatites and aplites: Their genetic and applied ore geology. *Ore Geol. Rev.* **2015**, *69*, 417–561. [[CrossRef](#)]
30. Guo, J.S.; Hua, R.M.; Huang, X.E. The Mineralization Characteristics and Prospecting Potential of the Deep Fine-Grained Tungsten-Molybdenum Granite in Southern Jiangxi. *China Tungsten Ind.* **2011**, *26*, 8–10, (In Chinese with English abstract). [[CrossRef](#)]
31. Xie, Y.L.; Li, L.M.; Guo, X.; Meffre, S.; Chang, Z.S.; Zhang, J.; Yao, Y.; Wang, A.G. Chronology, petrochemistry of fine-grained granite and their implication to Mo-Cu mineralization in Xichong Mo deposit, Anhui Province, China. *Acta Petrol. Sin.* **2015**, *31*, 1929–1942, (In Chinese with English abstract). [[CrossRef](#)]
32. Zhong, W.L.; Liu, J.D.; Zhang, C.J.; Li, Y.G. Characteristics of fine grain granitic rock and its metallogenic significance for Zhujiding copper deposit in western Sichuan, China. *Geol. Bull. China.* **2010**, *29*, 771–778, (In Chinese with English abstract).
33. Ren, H.; Wu, J.; Ye, X.; Ling, H.; Chen, P. Zircon U-Pb Age and Geochemical Characteristics of Peraluminous Fine-Grained Granite in Western Part of the Fucheng Pluton, Jiangxi Province. *Geol. J. China Univ.* **2013**, *19*, 327–345, (In Chinese with English abstract).
34. Yu, H.; Cai, Y.Q.; Li, W.L.; Huang, G.L.; Pang, Y.Q.; Jiang, W.B.; Zhang, C. LA-ICP-MS Zircon U-Pb Ages of the Fine-grained Granites in Gaoping Area, South Zhuguang Mountains and Their Geological Significances. *Geol. Rev.* **2017**, *63*, 781–792. [[CrossRef](#)]
35. Xie, Y.L.; Tang, Y.W.; Li, Y.X.; Qiu, L.M.; Liu, B.S.; Li, Y.; Zhang, X.X.; Han, Y.D.; Jiang, Y.C. Petrochemistry, chronology and ore-forming geological significance of fine crystalline granite in Anji polymetallic deposit of Zhejiang Province. *Miner. Depos.* **2012**, *31*, 891–902, (In Chinese with English abstract).
36. Yan, L.J.; Zhu, G.; Lin, S.Z.; Zhao, T. Neotectonic activity and formation mechanism of the Yishu Fault Zone. *Sci. China Earth Sci.* **2014**, *57*, 614–629. [[CrossRef](#)]
37. Wang, Z.L.; Yang, L.Q.; Deng, J.; Santosh, M.; Zhang, H.F.; Liu, Y.; Li, R.H.; Huang, T.; Zheng, X.L.; Zhao, H. Gold-hosting high Ba-Sr granitoids in the Xincheng gold deposit, Jiaodong Peninsula, East China: Petrogenesis and tectonic setting. *J. Asian Earth Sci.* **2014**, *95*, 274–299. [[CrossRef](#)]
38. Li, S.; Xiao, Y.; Liu, D.; Chen, Y.; Ge, N.; Zhang, Z.; Sun, S.; Cong, B.; Zhang, R.; Hart, S.R.; et al. Collision of the North China and Yangtze blocks and formation of coesite-bearing eclogites: Timing and processes. *Chem. Geol.* **1993**, *109*, 89–111. [[CrossRef](#)]
39. Zheng, Y.F.; Fu, B.; Gong, B.; Li, L. Stable isotope geochemistry of ultrahigh pressure metamorphic rocks from the Dabie-Sulu orogen in China: Implications for geodynamics and fluid regime. *Earth-Sci. Rev.* **2003**, *62*, 105–161. [[CrossRef](#)]
40. Tang, J.; Zheng, Y.F.; Wu, Y.B.; Gong, B.; Zha, X.; Liu, X. Zircon U-Pb age and geochemical constraints on the tectonic affinity of the Jiaodong terrane in the Sulu orogen, China. *Precambrian Res.* **2008**, *161*, 389–418. [[CrossRef](#)]
41. Hacker, B.R.; Wallis, S.R.; Ratschbacher, L.; Grove, M.; Gehrels, G. High-temperature geochronology constraints on the tectonic history and architecture of the ultrahigh-pressure Dabie-Sulu Orogen. *Tectonics* **2006**, *25*, 5006. [[CrossRef](#)]
42. Yang, L.Q.; Dilek, Y.; Wan, Z.L.; Weinberg, R.F.; Liu, Y. Late Jurassic, high Ba-Sr Linglong granites in the Jiaodong Peninsula, east China: Lower crustal melting products in the eastern North China craton. *Geol. Mag.* **2018**, *55*, 1040–1062. [[CrossRef](#)]
43. Hu, F.F.; Fan, H.R.; Yang, J.H.; Wan, Y.S.; Liu, D.Y.; Zhai, M.G.; Jin, C.W. Mineralizing age of the Rushan lode gold deposit in the Jiaodong Peninsula: SHRIMP U-Pb dating on hydrothermal zircon. *Chin. Sci. Bull.* **2004**, *49*, 1629–1636. [[CrossRef](#)]
44. Guo, J.H.; Chen, F.K.; Zhang, X.M.; Siebel, W.; Zhai, M.G. Evolution of syn- to postcollisional magmatism from north Sulu UHP belt, eastern China: Zircon U-Pb geochronology. *Acta Petrol. Sin.* **2005**, *21*, 1281–1301, (In Chinese with English abstract). [[CrossRef](#)]

45. Goss, S.C.; Wilde, S.A.; Wu, F.Y.; Yang, J.H. The age, isotopic signature and significance of the youngest Mesozoic granitoids in the Jiaodong Terrane, Shandong Province, North China Craton. *Lithos* **2010**, *120*, 309–326. [[CrossRef](#)]
46. Hu, F.F.; Fan, H.R.; Yang, K.F.; Shen, K.; Zhai, M.G.; Jin, C.W. Fluid inclusions in the Denggezhuang lode gold deposit at Muping, Jiaodong Peninsula. *Acta Petrol. Sin.* **2007**, *23*, 2155–2164, (In Chinese with English abstract). [[CrossRef](#)]
47. Zhang, L.; Yang, L.Q.; Weinberg, R.F.; Groves, D.I.; Wang, Z.L.; Li, G.W.; Liu, Y.; Zhang, C.; Wang, Z.K. Anatomy of a world-class epizonal orogenic-gold system: A holistic thermochronological analysis of the Xincheng gold deposit, Jiaodong Peninsula, eastern China. *Gondwana Res.* **2019**, *70*, 50–70. [[CrossRef](#)]
48. Burke, E.A. Raman microspectrometry of fluid inclusions. *Lithos* **2001**, *55*, 139–158. [[CrossRef](#)]
49. Liu, H.B.; Jin, G.S.; Li, J.J.; Han, J.; Zhang, J.F.; Zhang, J.; Zhong, F.W.; Guo, D.Q. Determination of stable isotope composition in uranium geological samples. *World Nucl. Geosci.* **2013**, *3*, 174–179, (In Chinese with English abstract). [[CrossRef](#)]
50. Burruss, R.C. Analysis of phase equilibria in C-O-H-S fluid inclusions. In *Fluid Inclusions: Applications to Petrology: A Short Course Sponsored by the Mineralogical Association of Canada and Held Immediately Prior to the 1981 Annual Meeting in Calgary, Alberta, May 7th–10th*; Mineralogical Association of Canada: Quebec City, QC, Canada, 1981; Volume 6, pp. 39–74.
51. Bakker, R.J. Package Fluids 1. Computer programs for analysis of fluid inclusion data and for modelling bulk fluid properties. *Chem. Geol.* **2003**, *194*, 3–23. [[CrossRef](#)]
52. Brown, P.E.; Hagemann, S.G. MacFlincor and its application to fluids in Archaean lode-gold deposits. *Geochim. Cosmochim. Acta* **1995**, *59*, 3943–3952. [[CrossRef](#)]
53. Thiéry, R.; Vidal, J.; Dubessy, J. Phase equilibria modelling applied to fluid inclusions: Liquid-vapour equilibria and calculation of the molar volume in the CO<sub>2</sub>-CH<sub>4</sub>-N<sub>2</sub> system. *Geochim. Cosmochim. Acta* **1994**, *58*, 1073–1082. [[CrossRef](#)]
54. Clayton, R.N.; O'Neil, J.R.; Mayeda, T.K. Oxygen isotope exchange between quartz and water. *J. Geophys. Res.* **1972**, *77*, 3057–3067. [[CrossRef](#)]
55. Taylor, H.P.; Sheppard, S.M.F. Igneous rocks: I. Processes of isotopic fractionation and isotope systematic. *Rev. Mineral.* **1986**, *16*, 227–271. [[CrossRef](#)]
56. Shmulovich, K.I.; Landwehr, D.; Simon, K.; Heinrich, W. Stable isotope fractionation between liquid and vapour in water–salt systems up to 600 °C. *Chem. Geol.* **1999**, *157*, 343–354. [[CrossRef](#)]
57. Driesner, T.; Seward, T.M. Experimental and simulation study of salt effects and pressure/density effects on oxygen and hydrogen stable isotope liquid-vapor fractionation for 4–5 mol aqueous NaCl and KCl solutions to 400 °C. *Geochim. Cosmochim. Acta* **2000**, *64*, 1773–1784. [[CrossRef](#)]
58. Peng, H.J.; Mao, J.W.; Hou, L.; Shu, H.Q.; Zhang, C.Q.; Liu, H.; Zhou, Y.M. Stable isotope and fluid inclusion constraints on the source and evolution of ore fluids in the Hongniu-Hongshan Cu skarn deposit, Yunnan Province, China. *Econ. Geol.* **2016**, *111*, 1369–1396. [[CrossRef](#)]
59. Taylor, B.E. Magmatic volatiles: Isotopic variation of C, H, and S. *Rev. Mineral.* **1986**, *16*, 185–226. [[CrossRef](#)]
60. Hedenquist, J.W.; Richards, J.P. The influence of geochemical techniques on the development of genetic models for porphyry copper deposits. *Rev. Econ. Geol.* **1998**, *10*, 235–256. [[CrossRef](#)]
61. Guo, L.N.; Zhang, C.; Song, Y.Z.; Chen, B.H.; Zhou, Z.; Zhang, B.L.; Xu, X.L.; Wang, Y.W. Hydrogen and oxygen isotopes geochemistry of the Wang'ershan gold deposit, Jiaodong. *Acta Petrol. Sin.* **2014**, *30*, 2481–2494, (In Chinese with English abstract).
62. Crawford, M.L. Phase equilibria in aqueous fluid inclusions. In *Fluid Inclusions: Applications to Petrology: A Short Course Sponsored by the Mineralogical Association of Canada and Held Immediately Prior to the 1981 Annual Meeting in Calgary, Alberta, May 7th–10th*; Mineralogical Association of Canada: Quebec City, QC, Canada, 1981; Volume 6, pp. 75–100.
63. Goldfarb, R.J.; Ayuso, R.; Miller, M.; Ebert, S.W.; Marsh, E.E.; Petsel, S.A.; Miller, L.D.; Bradley, D.; Johnson, C.; Johnson, C.; et al. The Late Cretaceous Donlin Creek gold deposit, Southwestern Alaska: Controls on epizonal ore formation. *Econ. Geol.* **2004**, *99*, 643–671. [[CrossRef](#)]
64. Chang, Z.S.; Large, R.R.; Maslennikov, V. Sulfur isotopes in sediment-hosted orogenic gold deposits: Evidence for an early timing and a seawater sulfur source. *Geology* **2008**, *36*, 971–974. [[CrossRef](#)]
65. Yang, L.Q.; Deng, J.; Wang, Z.L.; Zhang, L.; Guo, L.N.; Song, M.C.; Zheng, X.L. Mesozoic gold metallogenic system of the Jiaodong gold province, eastern China. *Acta Petrol. Sin.* **2014**, *30*, 2447–2467, (In Chinese with English abstract).
66. Zartman, R.E.; Haines, S.M. The plumbotectonic model for Pb isotopic systematics among major terrestrial reservoirs—A case study for bi-directional transport. *Geochim. Cosmochim. Acta* **1988**, *52*, 1327–1339. [[CrossRef](#)]
67. Ramboz, C.; Schnapper, D.; Dubessy, J. The P-V-T-X-fO<sub>2</sub> evolution of H<sub>2</sub>O-CO<sub>2</sub>-CH<sub>4</sub>-bearing fluids in a wolframite vein: Reconstruction from fluid inclusion studies. *Geochim. Cosmochim. Acta* **1985**, *49*, 205–219. [[CrossRef](#)]
68. Samson, I.M. Fluid evolution and mineralization in a subvolcanic granite stock: The Mount Pleasant W-Mo-Sn deposits, New Brunswick, Canada. *Econ. Geol.* **1990**, *85*, 145–163. [[CrossRef](#)]
69. O'Reilly, C.; Gallagher, V.; Feely, M. Fluid inclusion study of the Ballinglen W-Sn-sulphide mineralization, SE Ireland. *Miner. Depos.* **1997**, *32*, 569–580. [[CrossRef](#)]
70. Landis, G.P.; Rye, R.O. Geologic, fluid inclusion and stable isotope studies of the Pasto Bueno tungsten base metal deposit, Northern Peru. *Econ. Geol.* **1974**, *69*, 1025–1059. [[CrossRef](#)]
71. Heinrich, C.A. The chemistry of hydrothermal tin (-tungsten) ore deposition. *Econ. Geol.* **1990**, *85*, 457–481. [[CrossRef](#)]
72. Bailly, L.; Grancea, L.; Kouzmanov, K. Infrared microthermometry and chemistry of wolframite from the baia sprie epithermal deposit. *Romania. Econ. Geol.* **2002**, *97*, 415–421. [[CrossRef](#)]

73. Beuchat, S.; Moritza, R.; Pettke, T. Fluid evolution in the W-Cu-Zn-Pb San Cristobal vein, Peru: Fluid inclusion and stable isotope evidence. *Chem. Geol.* **2004**, *210*, 201–224. [[CrossRef](#)]
74. Higgins, N.C.; Kerrich, R. Progressive <sup>18</sup>O depletion during CO<sub>2</sub> separation from a carbon dioxide-rich hydrothermal fluid: Evidence from the Grey River tungsten deposit, Newfoundland. *Can. J. Earth Sci.* **1982**, *19*, 2247–2257. [[CrossRef](#)]
75. Ramboz, C.; Pichavant, M.; Weisbrod, A. Fluid immiscibility in natural processes: Use and misuse of fluid inclusion data. II. Interpretation of fluid inclusion data in terms of immiscibility. *Chem. Geol.* **1982**, *37*, 29–48. [[CrossRef](#)]
76. Seal, R.R., II; Clark, A.H.; Morrissey, C.J. Stockwork tungsten (scheelite)-molybdenum mineralization, Lake George, Southwestern New Brunswick. *Econ. Geol.* **1987**, *82*, 1259–1282. [[CrossRef](#)]
77. Lynch, J.V.G. Hydrothermal alteration, veining, and fluid inclusion characteristics of the Kalzas wolframite deposit. *Yukon. Can. J. Earth Sci.* **1989**, *26*, 2106–2115. [[CrossRef](#)]
78. Graupner, T.; Kempe, U.; Dombon, E. Fluid regime and ore formation in the tungsten deposits of Kyzyltau (Mongolian Altai) evidence for fluid variability in tungsten-tin ore systems. *Chem. Geol.* **1999**, *154*, 29–40. [[CrossRef](#)]
79. Wang, X.D.; Ni, P.; Yuan, S.D.; Wu, S.H. Fluid inclusion studies of the Huangsha quartz-vein type tungsten deposit. *Jiangxi Prov. Acta Petrol. Sin.* **2012**, *28*, 122–132. [[CrossRef](#)]
80. Kelly, W.C.; Rye, R.O. Geologic fluid inclusion and stable isotope studies of the tin-tungsten deposits of Panasqueira. *Portugal. Econ. Geol.* **1979**, *74*, 1721–1822. [[CrossRef](#)]
81. Polyá, D.A. Chemistry of the main-stage ore-forming fluids of the Panasqueira W-Cu(Ag)–Sn deposit. *Port. Implic. Models Ore Genes. Econ. Geol.* **1989**, *84*, 1134–1152. [[CrossRef](#)]
82. Clark, A.H.; Kontak, D.J.; Farrar, E. The San Judas Tadeo W (-Mo-Au) deposit: Permian lithophile mineralization in southeastern Peru. *Econ. Geol.* **1990**, *85*, 1651–1668. [[CrossRef](#)]
83. Cattalani, S.; Williams-Jones, A.E. C-O-H-N fluid evolution at Saint-Robert, Quebec: Implications for W-Bi-Ag mineral deposition. *Can. Mineral.* **1991**, *29*, 435–452.
84. Ni, P.; Chi, Z.; Pan, J.Y. An integrated investigation of ore-forming fluid evolution in porphyry and epithermal deposits and their implication on exploration. *Front. Earth Sci.* **2020**, *27*, 60–78. [[CrossRef](#)]
85. Dressel, B.C.; Chauvet, A.; Trzaskos, B.; Biondi, J.C.; Bruguier, O.; Monié, P.; Villanova, S.N.; Newton, J.B. The Passa Três lode gold deposit (Paraná State, Brazil): An example of structurally-controlled mineralisation formed during magmatic-hydrothermal transition and hosted within granite. *Ore Geol. Rev.* **2018**, *102*, 701–727. [[CrossRef](#)]
86. Pirajno, F. *Hydrothermal Processes and Mineral Systems*; Springer: Berlin, Germany, 2009; pp. 205–354.
87. Robert, F. Syenite-associated disseminated gold deposits in the Abitibi greenstone belt, Canada. *Miner. Deposita* **2001**, *36*, 503–516. [[CrossRef](#)]
88. Jeremy, P. Richards; Robert Kerrich. The Porgera gold mine, Papua New Guinea; magmatic hydrothermal to epithermal evolution of an alkalic-type precious metal deposit. *Econ. Geol.* **1993**, *88*, 1017–1052. [[CrossRef](#)]
89. Mustard, R. Granite-hosted gold mineralization at Timbarra, northern New South Wales, Australia. *Miner. Deposita* **2001**, *36*, 542–562. [[CrossRef](#)]
90. Thompson, J.F.H.; Sillitoe, R.H.; Baker, T.; Lang, J.R.; Mortensen, J.K. Intrusion-related gold deposits associated with tungsten-tin provinces. *Miner. Deposita* **1999**, *34*, 323–334. [[CrossRef](#)]
91. Baker, T. Emplacement depth and carbon dioxide-rich fluid inclusions in intrusion-related gold deposits. *Econ. Geol.* **2002**, *97*, 1111–1117. [[CrossRef](#)]